Journal of Geophysical Research

Supporting information for

A Late Cretaceous-Eocene Geomagnetic Polarity Time Scale (MQSD20) that steadies spreading rates on multiple mid-ocean ridge flanks

A. Malinverno[1], K. W. Quigley[2], A. Staro[3], and J. Dyment[4]

[1]Lamont-Doherty Earth Observatory of Columbia University, Palisades, New York, USA

[2]Brown University, Providence, Rhode Island, USA

[3]Dipartimento di Scienze della Terra, Università degli Studi di Milano, Italy

[4]Université de Paris, Institut de Physique du Globe de Paris, CNRS, Paris, France

Contents of this file

Introduction

The Supporting Information includes text that details the implementation of Markov chain Monte Carlo (MCMC) sampling for two cases. Text S1 describes the sampling of block model distances along a ship track projected onto a flow line to fit measured magnetic anomalies. Text S2 describes the sampling of ages in a geomagnetic polarity time scale (GPTS) to minimize global variations in spreading rate and fit radioisotopic dates. The notation used in the text is listed in Table S1. Figures S1 to S16 are maps showing the locations of original and projected ship tracks and of selected polarity block boundaries in 13 ridge flank regions. Figure S17 to S29 plot a comparison of half-spreading rates in 13 ridge flank regions for three GPTSs: MQSD20 (this paper), CK95 (Cande & Kent 1992, 1995), and GTS12 (Ogg 2012).

Text S1. MCMC sampling of block model distances

The parameter vector

This sampling generates a number of block model distances (BMDs) that result in a good fit between observed and modeled magnetic anomalies in each of the projected ship tracks. In any given ship track, the parameter vector **m** includes

- A vector of BMDs for the anomalies in the track.
- The standard deviation σ_e of the misfits between observed and predicted magnetic anomalies. This hyperparameter (Gelman et al. 2004; Malinverno & Briggs 2004) is included in **m** because it is not known a priori. Sampling will determine how closely the magnetic anomaly data can be fitted.
- A set of nodes spaced every ~50 km that define a multiplier for the magnetic anomaly amplitudes (Figure 2 in the main text). Adjusting the amplitude of the predicted anomalies to match those observed is necessary to prevent the Monte Carlo algorithm from sampling unrealistically narrow polarity blocks in areas of low-amplitude anomalies (see the main text).

Data and likelihood function

The observed data **d** in the likelihood function are the magnetic anomaly data, highpass filtered to eliminate long-wavelength components that are not generated by magnetized crustal blocks and normalized to zero mean and unit variance. The predicted data $\mathbf{d}_{\mathsf{pred}}$ are magnetic anomalies computed by upward continuation of crustal blocks of constant positive or negative magnetization. The horizontal distances to the block boundaries are defined by the BMDs, and the blocks are assumed to be be between 5,000 m and 5,500 m below sea level. The predicted anomalies are phase-shifted for the given skewness angle, multiplied by the anomaly multiplier values, and normalized. The likelihood function is defined as a multivariate normal PDF:

$$p(\mathbf{d}|\mathbf{m}) = (2\pi\sigma_e^2)^{-N_d/2} \exp\left[-\frac{1}{2\sigma_e^2}(\mathbf{d}-\mathbf{d}_{\mathsf{pred}})^{\mathsf{T}}(\mathbf{d}-\mathbf{d}_{\mathsf{pred}})\right], \quad (1)$$

where $\mathbf{x}^{\mathsf{T}}$ denotes the transpose of the vector **x**, N_d is the length of the data vectors, and σ_e^2 is the variance of the misfits between observed and predicted data.

Generating candidate parameter vectors

The generation of candidate parameters $\mathbf{m}^*$ starts by choosing at random between one of the BMDs (with probability 0.4), one of the nodes of the magnetic anomaly multipliers (probability 0.4), the anomaly skewness angle (probability 0.1), or the standard deviation of the data misfits σ_e (probability 0.1). A candidate value for the parameter to perturb is then chosen at random from its prior distribution. The prior distributions of the parameters in **m** are uniform between reasonable minimum and maximum bounds. Each of the BMDs has a uniform prior between the distances to the surrounding BMDs ±1 km (to avoid zero-width magnetic blocks). The anomaly multiplier nodes have a uniform prior between 0.3 and 1.7. The skewness angle has a uniform prior between bounds of ±30° around the initial value. The misfit standard deviation has a log-uniform prior between a minimum equal to 1/3 of σ_e for the initial BMDs and a maximum of 1 (a very poor fit for standardized data).

MCMC sampling

Starting the sampling from an initial value of the parameters that approximately fits the data, the MCMC algorithm generates a sample of BMDs that fit the observed magnetic anomalies as closely as possible (see Figure 2 in the main text). The MCMC algorithm was run for 20,000 iterations, and the sampled BMDs were saved every 50 iterations to result in a final sample of 400 BMDs in each ship track. (As only one parameter in the candidate vector is changed at each iteration, consecutive samples are very similar and it is unnecessary to save them all.) The mean and standard deviation of the sampled values define a best value and an uncertainty for the BMDs along the projected ship track, which are the input to the construction of summary BMDs in each ridge flank region (see the main text). Maps of the 154 original and projected ship tracks and geographic positions of selected polarity block boundaries in each of the original tracks are in Figures S1-S16.

Text S2. MCMC sampling of the Geomagnetic Polarity Time Scale

The parameter vector

This sampling generates a number of geomagnetic polarity time scales (GPTSs) that fit a set of radioisotopic dates (see Table 3 in the main text) and that minimize the global variation of spreading rates. The parameter vector $\mathbf{m}$ includes

- A GPTS vector $\mathbf{t}$ of 59 ages of polarity chron boundaries (from C13ny to C34ny).
- A vector $\mathbf{c}$ of 13 coefficients of variation (CVs) that are the ratio between the standard deviation and the average of the spreading rates; these CVs quantify the long-term variations of spreading rate in each of the mid-ocean ridge flank regions.

The CVs are the ratio of the standard deviation over the average spreading rate. There are two major sources of variability in the spreading rates calculated over a ridge flank for a given GPTS: short-term variations due to uncertainties in the estimated BMDs and long-term changes due to changes in large-scale plate motion. Both these sources of variation need to be taken into account in the calculation of the likelihood. The size of long-term spreading rate variations will be different on different mid-ocean ridge flanks, and the 13 CVs in the parameter vector are hyperparameters that are not assumed to be known a priori (Gelman et al. 2004; Malinverno & Briggs 2004). Sampling will determine the magnitude of the long-term spreading rate variations over each ridge flank region.

The observed data vector in the likelihood

The vector of observed data $\mathbf{d}$ in the likelihood function is the combination of several data vectors:

- Thirteen vectors of spreading rates $\mathbf{u}^{[j]}$ ($j = 1, 2, \ldots, 13$) in each of the mid-ocean ridge flank regions computed from the BMDs in $\mathbf{b}$ and the GPTS ages in $\mathbf{t}$.
- A vector $\mathbf{r}$ of 16 radioisotopic dates from magnetostratigraphy (Table 3 in the main text).

As the uncertainties of spreading rates over each of the 13 ridge flank regions and the uncertainties of radioisotopic dates are uncorrelated, we can write the total likelihood as the product of each likelihood:

$$p(\mathbf{d}|\mathbf{m}) = p(\mathbf{u}^{[1]}|\mathbf{m})p(\mathbf{u}^{[2]}|\mathbf{m}) \ldots p(\mathbf{u}^{[13]}|\mathbf{m})p(\mathbf{r}|\mathbf{m}). \quad (2)$$

Likelihood of spreading rates

We describe here the likelihood function of spreading rates in a mid-ocean ridge flank region. For simplicity of notation, we omit in this section the superscript $[j]$ that denotes the ridge flank region (e.g., we write $\mathbf{u}^{[j]}$ as $\mathbf{u}$). The likelihood for a vector $\mathbf{u}$ of N_u spreading rates in the j-th ridge flank region is a multivariate normal PDF with a mean equal to a weighted average spreading rate $\overline{u}$ and a covariance matrix $\mathbf{C}_u$ as in

$$p(\mathbf{u}|\mathbf{m}) = [(2\pi)^{N_u} \det \mathbf{C}_u]^{-1/2} \exp\left[-\frac{1}{2}(\mathbf{u}-\overline{u})^{\mathsf{T}}\mathbf{C}_u^{-1}(\mathbf{u}-\overline{u})\right], \tag{3}$$

The half-spreading rates in the vector $\mathbf{u}$ of Equation 3 are computed from the vector $\mathbf{b}$ of BMDs in the j-th ridge flank region and the GPTS in $\mathbf{t}$ as

$$u_i = \frac{b_{i+1} - b_i}{t_{i+1} - t_i}, \tag{4}$$

where the ages t_i are the ages of the GPTS chron boundaries that correspond to the BMDs in $\mathbf{b}$. The spreading rate calculation can be written as

$$\mathbf{u} = \mathbf{H}\,\mathbf{b}, \tag{5}$$

where $\mathbf{H}$ is a matrix that depends on the GPTS in $\mathbf{t}$

$$\mathbf{H} = \begin{bmatrix} -\dfrac{1}{t_2 - t_1} & \dfrac{1}{t_2 - t_1} & 0 & \dots & 0 & 0 \\ 0 & -\dfrac{1}{t_3 - t_2} & \dfrac{1}{t_3 - t_2} & \dots & 0 & 0 \\ \vdots & \vdots & \vdots & \ddots & \vdots & \vdots \\ 0 & 0 & 0 & \dots & -\dfrac{1}{t_{N_u+1} - t_{N_u}} & \dfrac{1}{t_{N_u+1} - t_{N_u}} \end{bmatrix}. \tag{6}$$

The covariance matrix $\mathbf{C}_u$ in Equation 3 accounts for two sources of variation in spreading rates over their average: uncertainties in the estimated BMDs in $\mathbf{b}$ and long-term variations in spreading rate quantified by the CVs in the vector $\mathbf{c}$. The uncertainties in the BMDs are described by a diagonal covariance matrix $\mathbf{C}_b$ that contains the variances obtained by assembling rescaled distances from projected ship tracks in the j-th ridge flank region (as described in the main text). From the properties of the multivariate normal distribution, the covariance matrix of the spreading rates $\mathbf{u}$ in Equation 5 that accounts for uncertainties in $\mathbf{b}$ is

$$\mathbf{C}_1 = \mathbf{H}\,\mathbf{C}_b\,\mathbf{H}^{\mathsf{T}}. \tag{7}$$

The weighted average spreading rate $\overline{u}$ in Equation 3 is obtained by weighing each value of spreading rate in $\mathbf{u}$ by the respective variance in the diagonal of $\mathbf{C}_1$.

The long-term variations of spreading rates are quantified by a diagonal covariance matrix $\mathbf{C}_2$ defined as

$$\mathbf{C}_2 = (c_j\overline{u})^2\mathbf{I}, \tag{8}$$

where c_j is the CV of spreading rates for the j-th ridge flank region and $\mathbf{I}$ is the $N_u \times N_u$ identity matrix.

The covariance matrix $\mathbf{C}_u$ in the likelihood of Equation 3 combines the two sources of spreading rate variation as

$$\mathbf{C}_u = \mathbf{C}_1 + \mathbf{C}_2. \tag{9}$$

Because of the structure of $\mathbf{H}$ (Equation 6), the matrix $\mathbf{C}_1$ is tridiagonal. We simplify the treatment and speed up calculations by discarding the off-diagonal elements of $\mathbf{C}_1$, so that $\mathbf{C}_u$ is also diagonal. This simplification does not impact significantly our results. We ran tests comparing Monte Carlo sampling results obtained using a tridiagonal or a diagonal $\mathbf{C}_1$, and found that they were very similar.

Likelihood of radioisotopic dates

The likelihood for a vector $\mathbf{r}$ of N_r measured radioisotopic dates is a multivariate normal PDF as in

$$p(\mathbf{r}|\mathbf{m}) = [(2\pi)^{N_r} \det \mathbf{C}_r]^{-1/2} \exp\left[-\frac{1}{2}(\mathbf{r} - \mathbf{r}_{\mathsf{pred}})^{\mathsf{T}} \mathbf{C}_r^{-1} (\mathbf{r} - \mathbf{r}_{\mathsf{pred}})\right]. \tag{10}$$

The vector of predicted dates $\mathbf{r}_{\mathsf{pred}}$ is obtained by linearly interpolating the GPTS ages in $\mathbf{t}$ to the stratigraphic positions of each date (Table 3 in the main text). The covariance matrix $\mathbf{C}_r$ is a diagonal matrix containing the total variances of each radioisotopic date. This total variance is the sum of the variance due to radioisotopic measurement uncertainty and the variance due to stratigraphic uncertainty (see the main text).

Generating candidate parameter vectors

Candidate parameters $\mathbf{m}^*$ are obtained by sampling at each iteration a candidate GPTS vector $\mathbf{t}^*$ and a candidate CV vector $\mathbf{c}^*$. The candidate GPTS is determined in two steps. The first step is to randomly choose a random perturbation Δt^* to be applied to a randomly chosen chron boundary. The perturbations Δt^* are designed to sample a lognormal prior PDF of chron durations. The parameters of the lognormal prior PDF are the mean and standard deviation of the logarithms of the C13-C33 chron durations in the CK95 time scale (Cande & Kent 1992, 1995), which are 0.7138 and 1.108, respectively, for chron durations in Ma. The second step is to choose one of two moves with equal probability: either add the perturbation Δt^* to a single chosen chron boundary or to a range of chron boundaries around the chosen one. In the latter case, the perturbation is distributed over nearby chron boundaries, following a Gaussian function that equals Δt^* at the chosen chron boundary and has a standard deviation of 1 Ma. This combination of local and extended GPTS perturbations improves the convergence of the MCMC algorithm to sample the posterior PDF of the GPTS.

Similarly, the candidate CV vector $\mathbf{c}^*$ is determined by adding a random perturbation Δc^* to a randomly chosen CV. The perturbations are designed to sample a prior PDF that is log-uniform in a broad interval of possible values of CV (0.02 to 0.8).

MCMC sampling and convergence assessment

To ensure that the MCMC algorithm converged to sampling the posterior PDF of the GPTS, we followed the recommended strategy outlined in Section 11.10 of Gelman et al. (2004). We ran 10 independent sampling chains, where each chain was started from a randomly perturbed version of

the CK95 GPTS, obtained by randomly changing the original chron boundary ages in an interval spanning ±30% of the chron durations. Each sampling chain ran for 200,000 iterations, and the sampled GPTSs were saved every 100 iterations.

To assess whether the chains converged to sample the posterior PDF, we computed for each sampled parameter of interest (GPTS ages in the vector $\mathbf{t}$) a $\widehat{R}$ statistic that compares the variance of a parameter sampled within each chain to the variance of samples between different chains. The practical recommendation of Gelman et al. (2004) is that convergence is reached if the $\widehat{R}$ statistic is less than 1.1 for all parameters. In our GPTS sampling, this threshold is reached after about 30,000 iterations. We conservatively discard the first 50,000 iterations in each chain and assemble all the remaining samples in all the chains to compute a mean and standard deviation of GPTS chron boundary ages and chron durations (Table 4 in the main text).

Table S1. List of symbols.

$\mathbf{b}$	Vector of block model distances (BMDs)
$\mathbf{c}$	Vector of coefficients of variation of spreading rates (CVs)
$\mathbf{C}_b$	Covariance matrix of BMD uncertainties
$\mathbf{C}_u$	Covariance matrix of spreading rate uncertainties
$\mathbf{C}_r$	Covariance matrix of radioisotopic date uncertainties
$\mathbf{d}$	Vector of observed data
$\mathbf{d}_{\mathsf{pred}}$	Vector of data predicted by the parameter vector $\mathbf{m}$
$\mathbf{m}$	Model parameter vector
$\mathbf{m}^*$	Candidate model parameter vector in MCMC sampling
$\mathbf{r}$	Vector of observed radioisotopic dates
$\mathbf{r}_{\mathsf{pred}}$	Vector of radioisotopic dates predicted by the parameter vector $\mathbf{m}$
$\mathbf{t}$	Vector of chron boundary ages in the GPTS
$\mathbf{u}$	Vector of spreading rates in a ridge flank region
$\overline{u}$	Weighted average of spreading rates in a ridge flank region
σ_e	Standard deviation of misfit between observed and predicted data

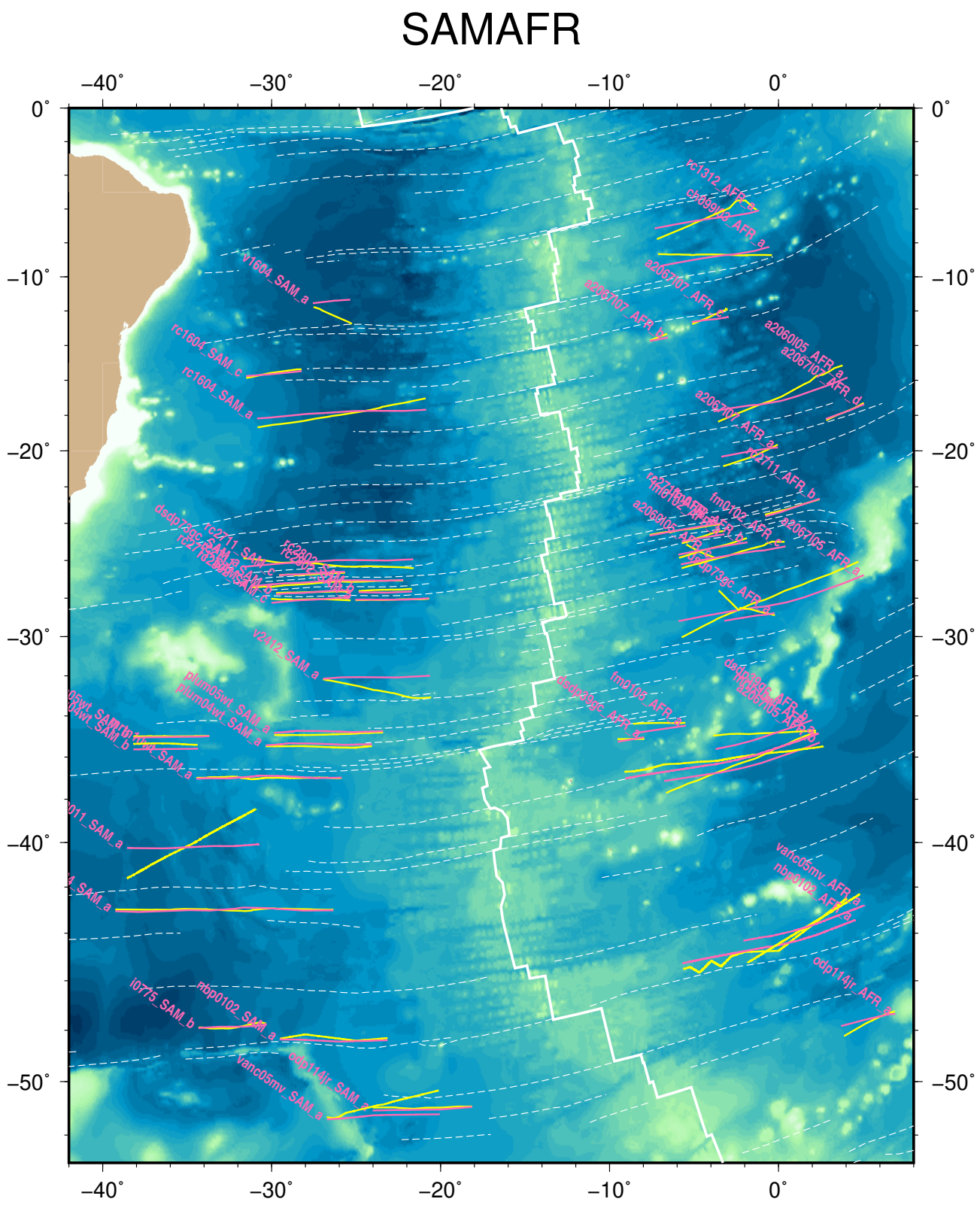

Figure S1. Original ship tracks (yellow) and tracks projected onto flow lines (magenta) in the SAMAFR-SAM and SAMAFR-AFR ridge flank regions.

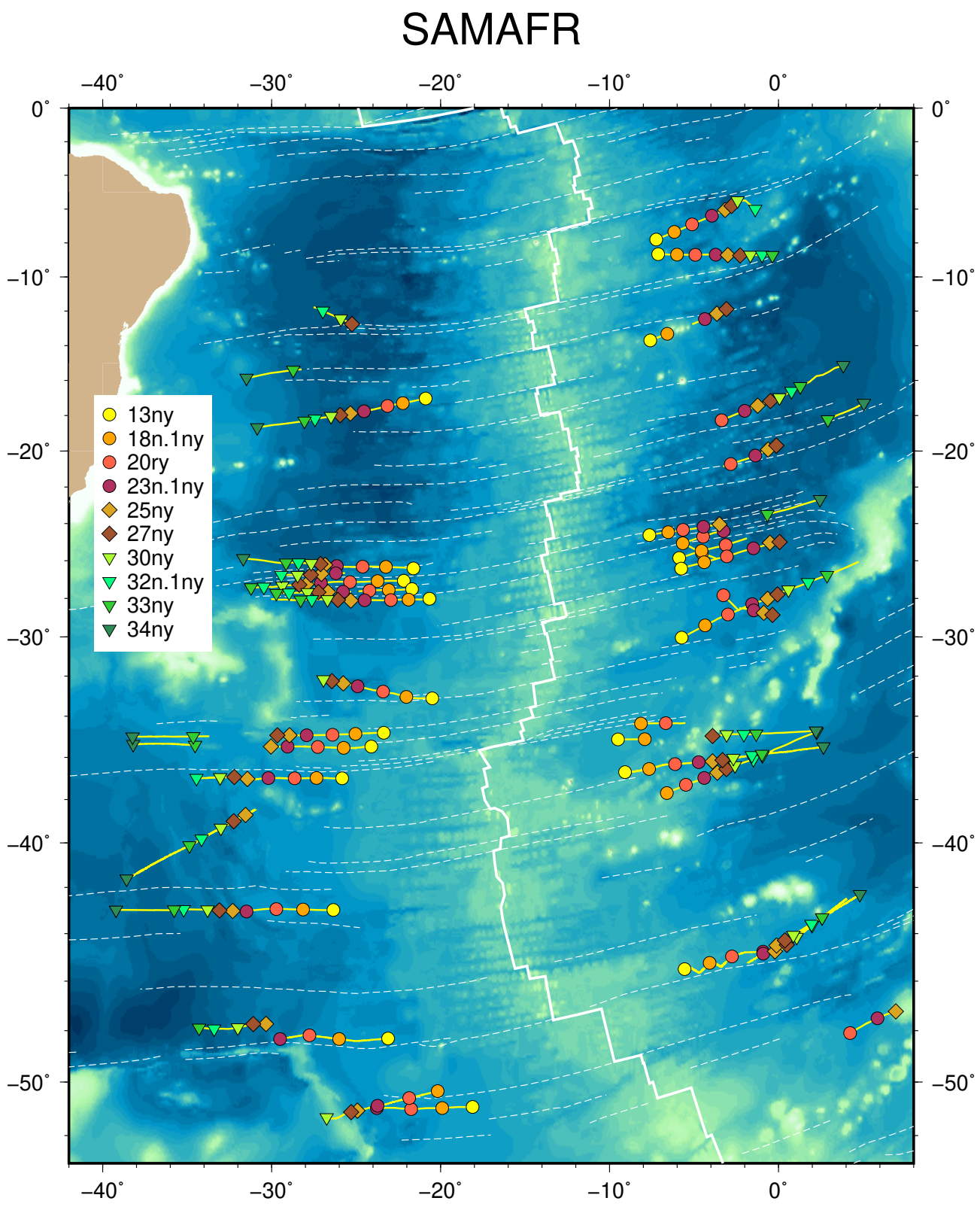

Figure S2. Location of selected magnetic block boundaries on original ship tracks in the SAMAFR-SAM and SAMAFR-AFR ridge flank regions.

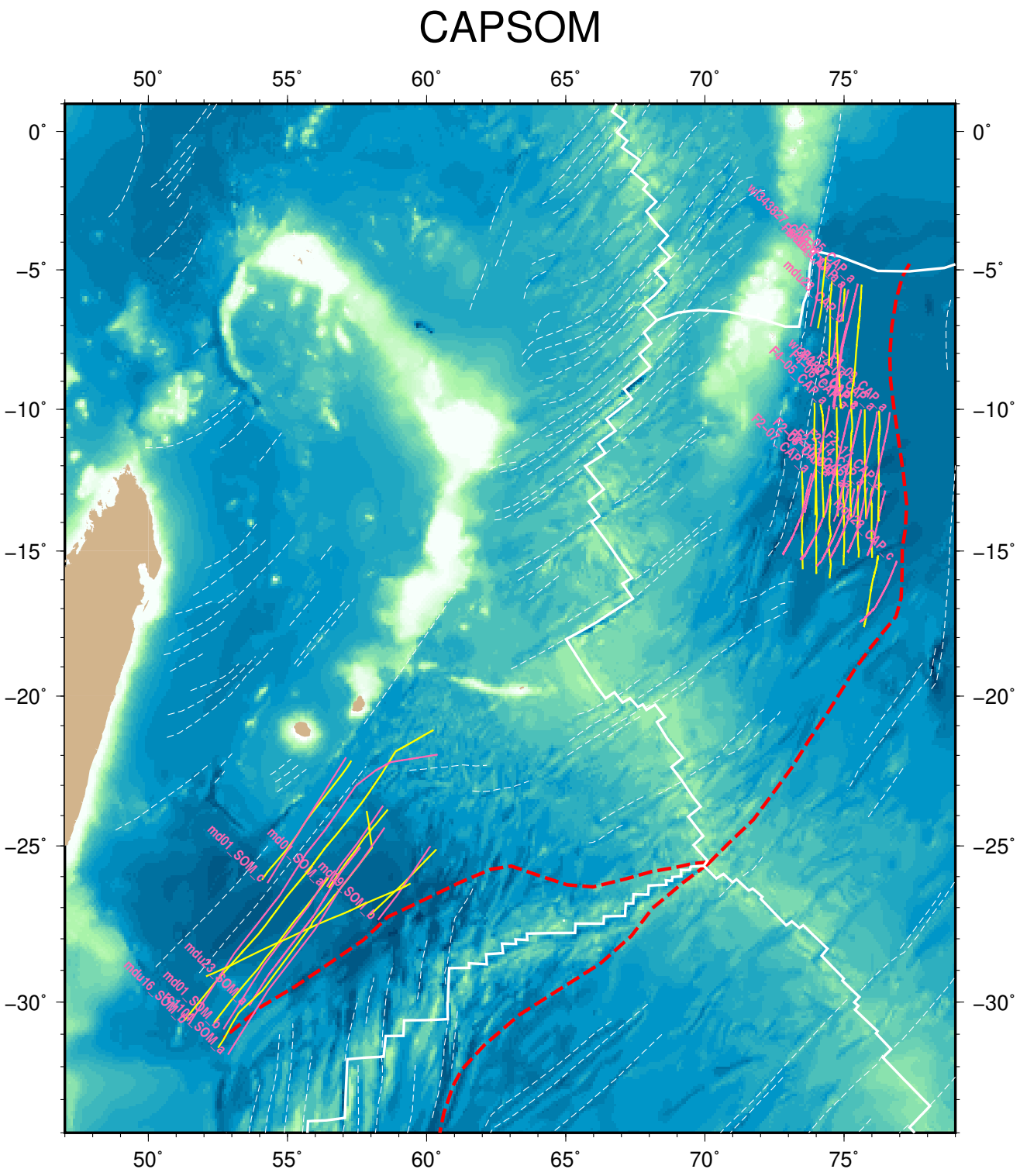

Figure S3. Original ship tracks (yellow) and tracks projected onto flow lines (magenta) in the CAPSOM-SOM and CAPSOM-CAP ridge flank regions.

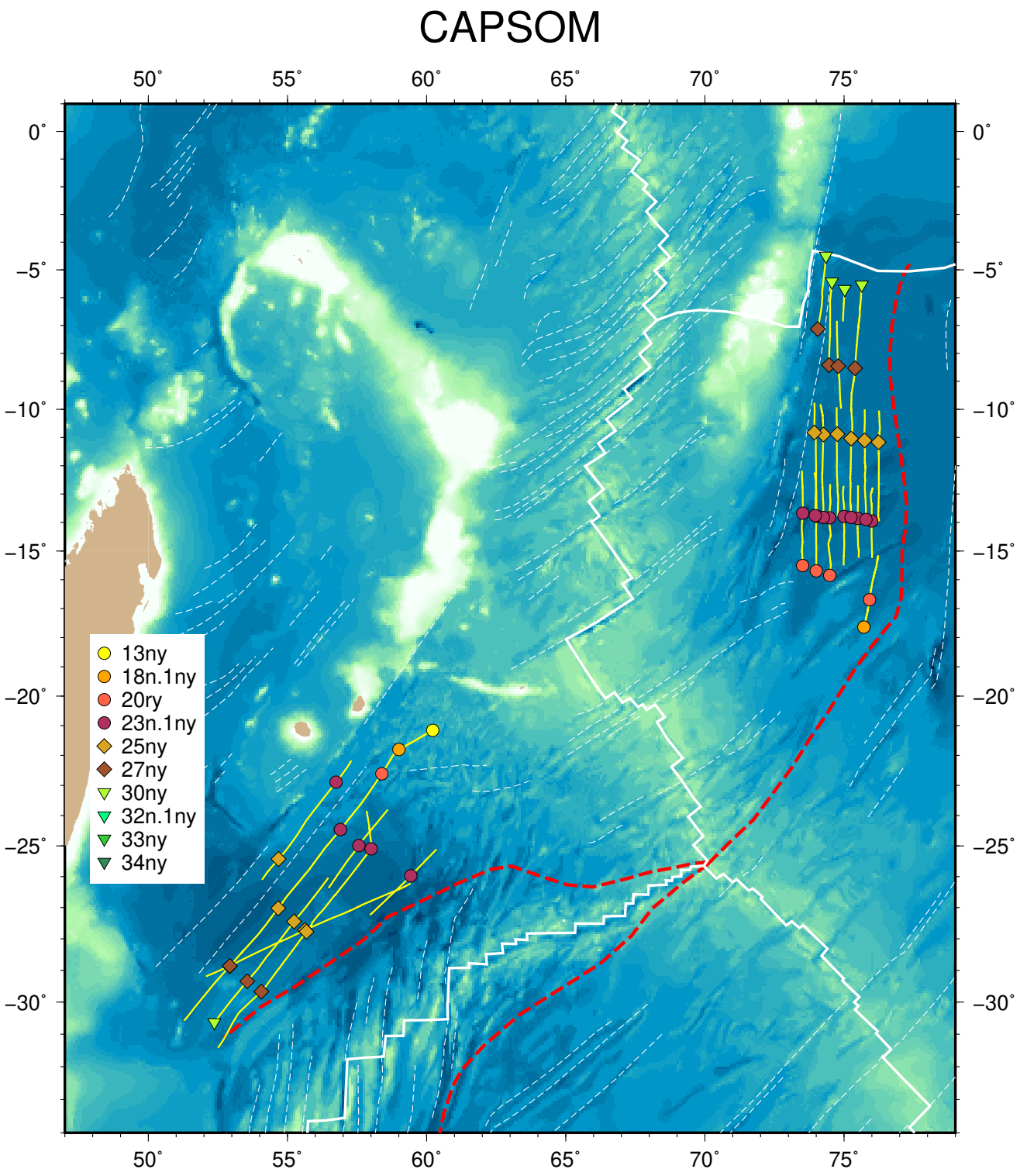

Figure S4. Location of selected magnetic block boundaries on original ship tracks in the CAPSOM-SOM and CAPSOM-CAP ridge flank regions.

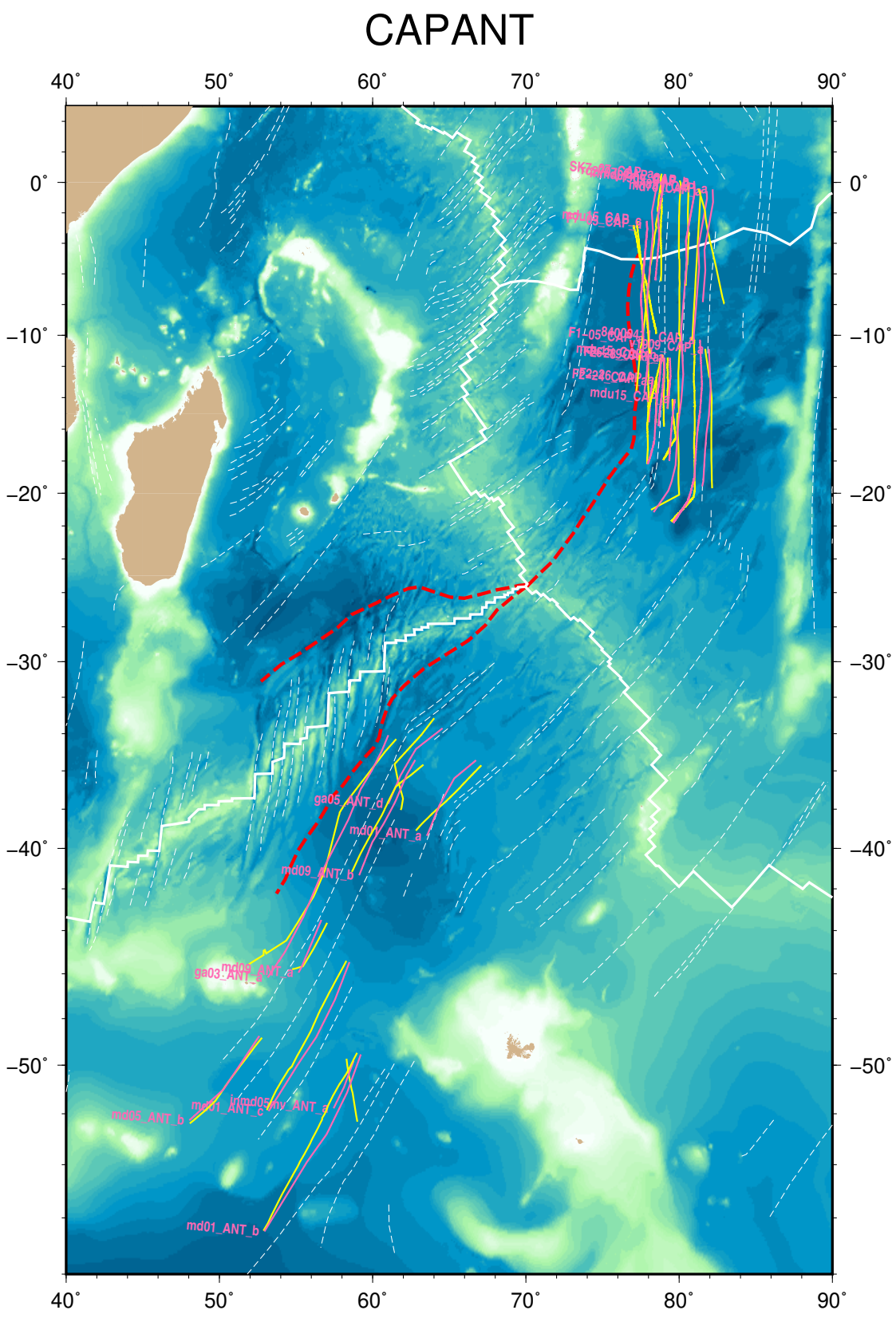

Figure S5. Original ship tracks (yellow) and tracks projected onto flow lines (magenta) in the CAPANT-ANT and CAPANT-CAP ridge flank regions.

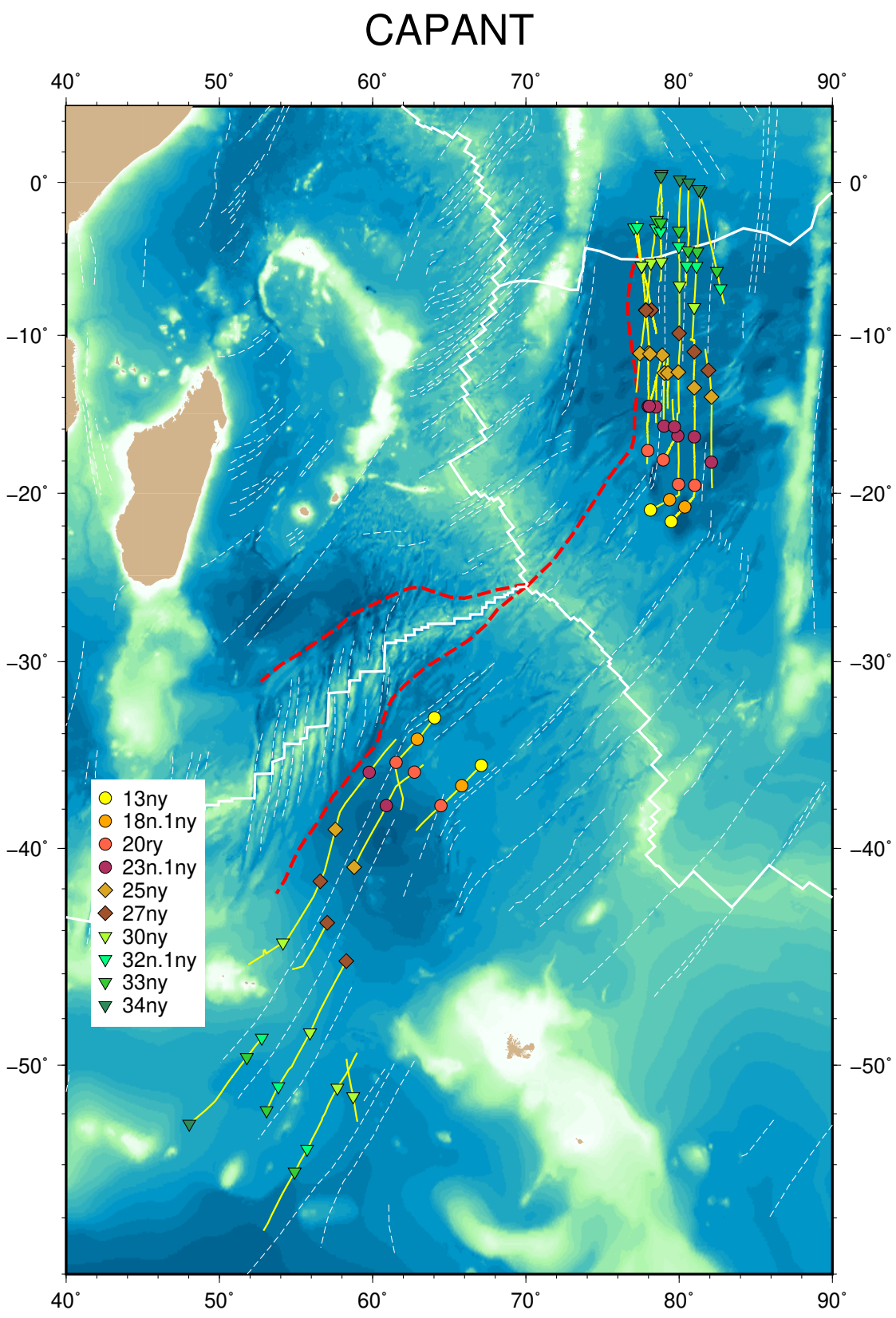

Figure S6. Location of selected magnetic block boundaries on original ship tracks in the CAPANT-ANT and CAPANT-CAP ridge flank regions.

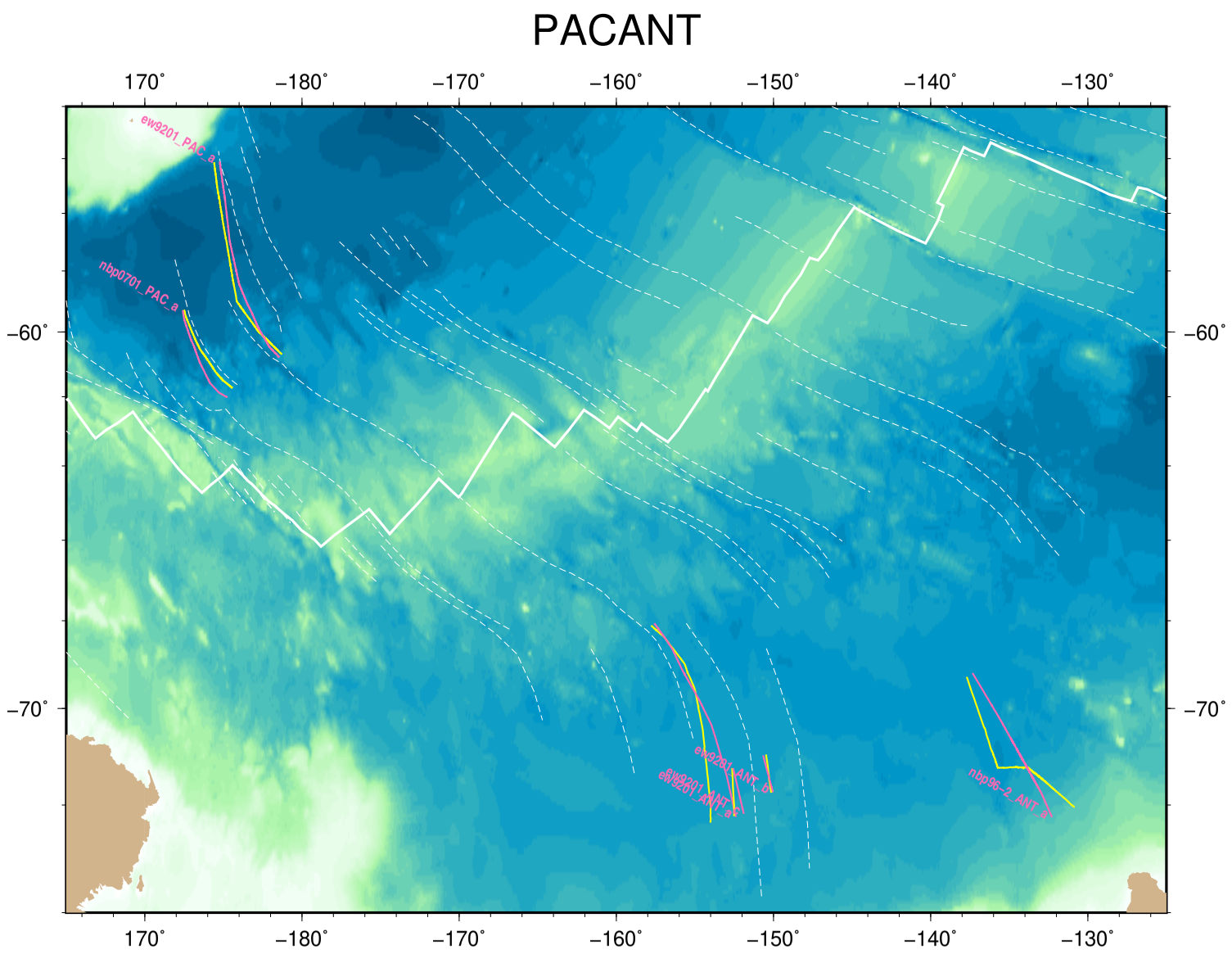

Figure S7. Original ship tracks (yellow) and tracks projected onto flow lines (magenta) in the PACANT-PAC and PACANT-ANT ridge flank regions.

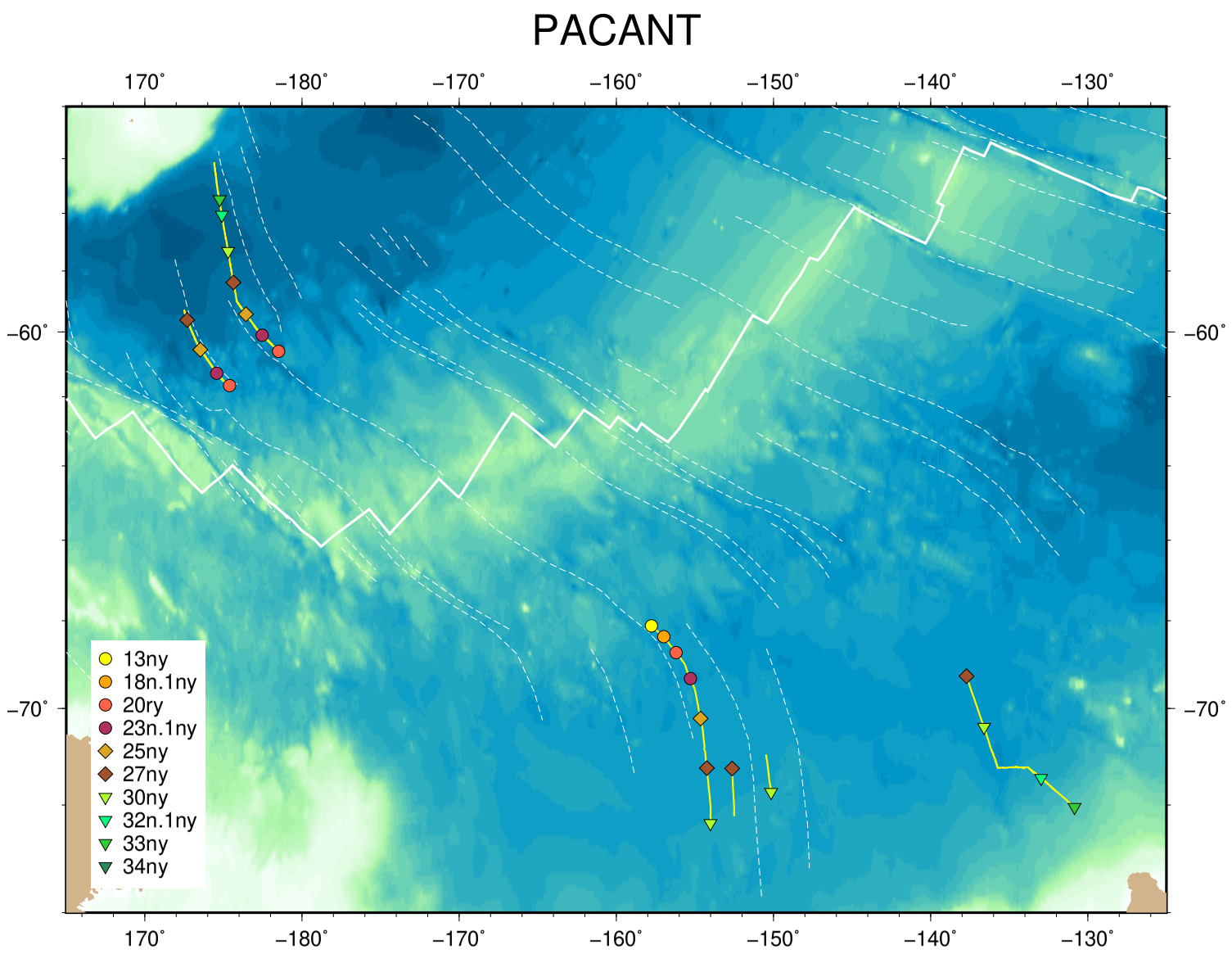

Figure S8. Location of selected magnetic block boundaries on original ship tracks in the PACANT-PAC and PACANT-ANT ridge flank regions.

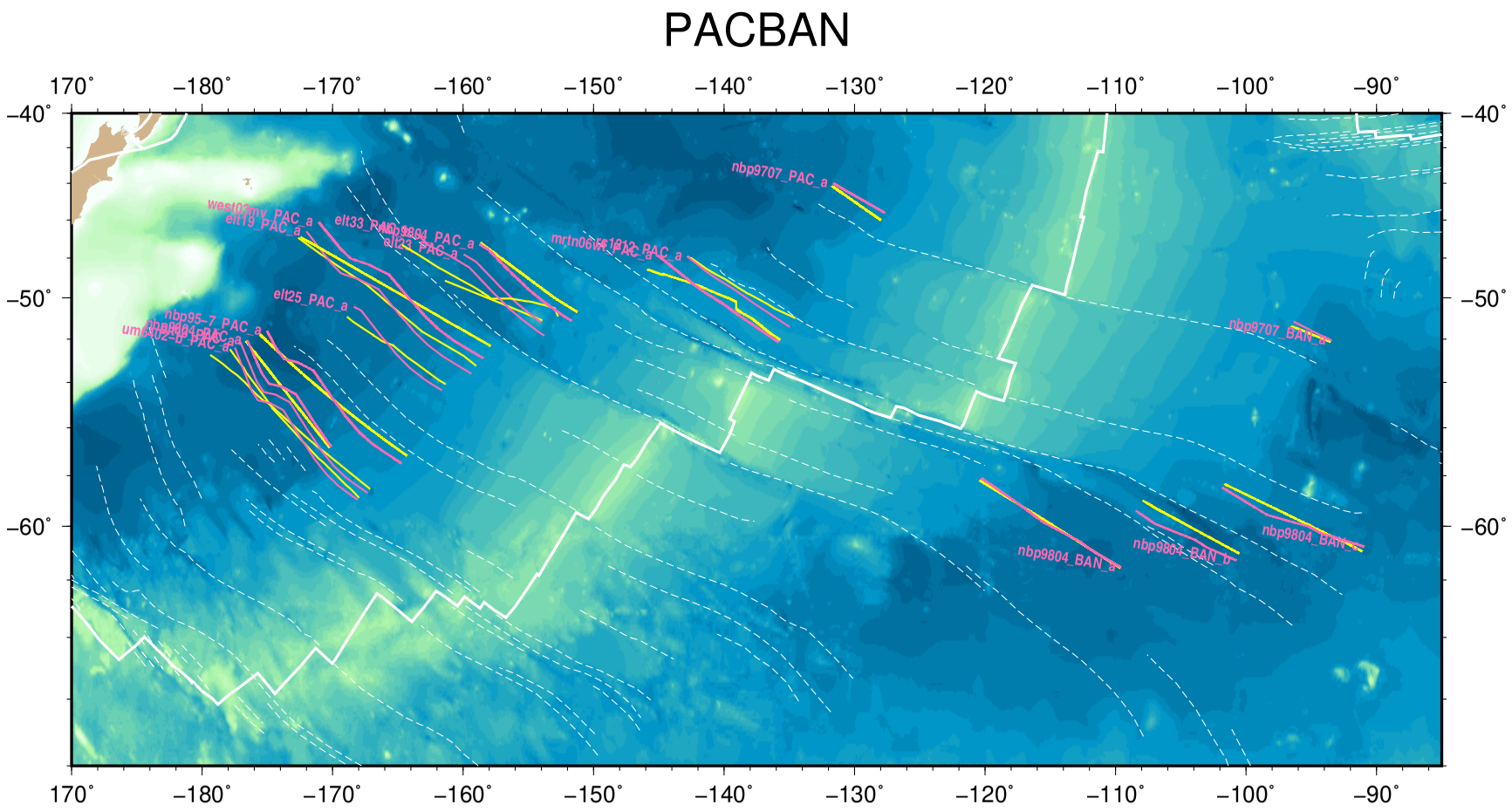

Figure S9. Original ship tracks (yellow) and tracks projected onto flow lines (magenta) in the PACBAN-PAC and PACBAN-BAN ridge flank regions.

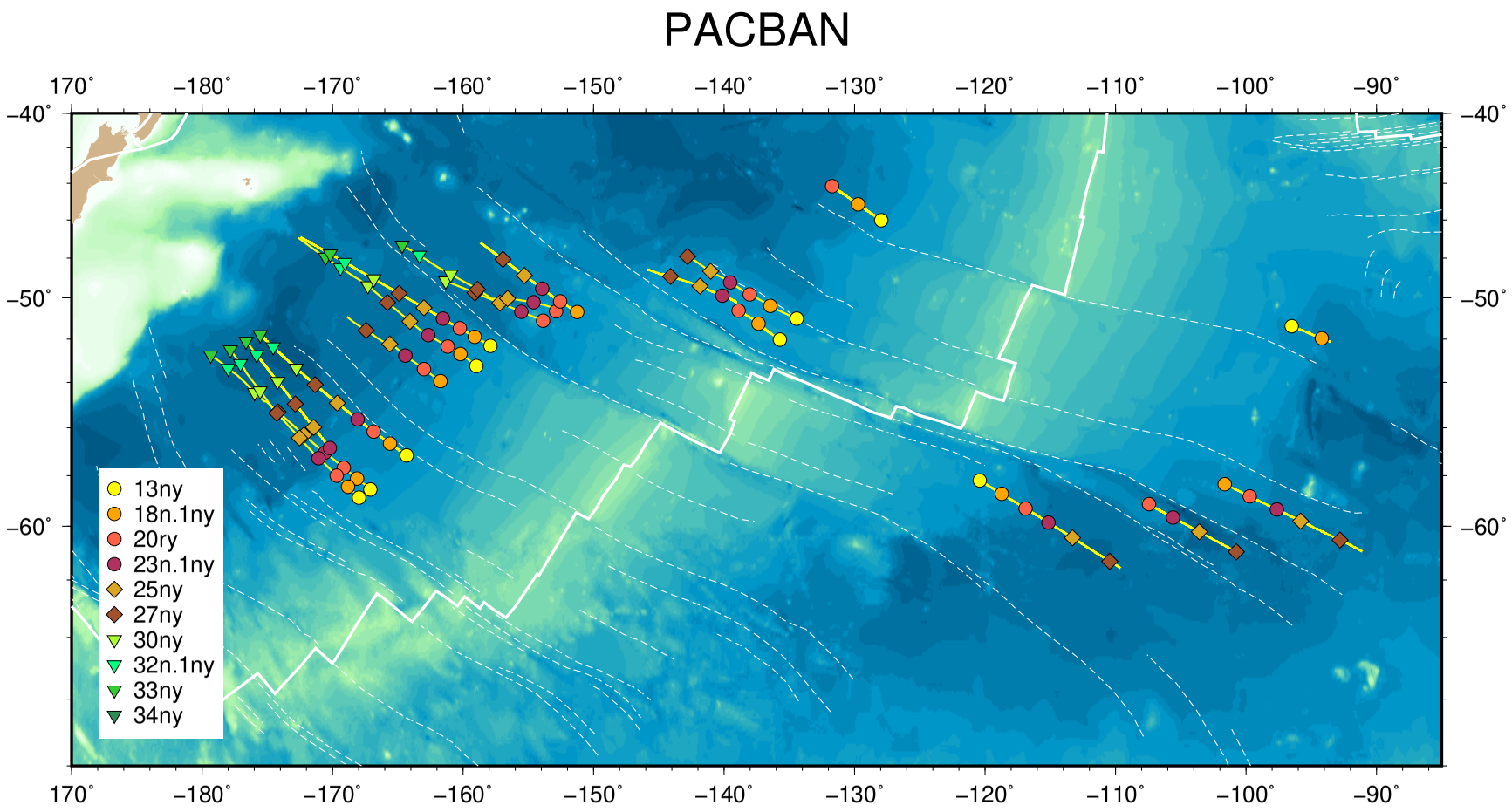

Figure S10. Location of selected magnetic block boundaries on original ship tracks in the PACBAN-PAC and PACBAN-BAN ridge flank regions.

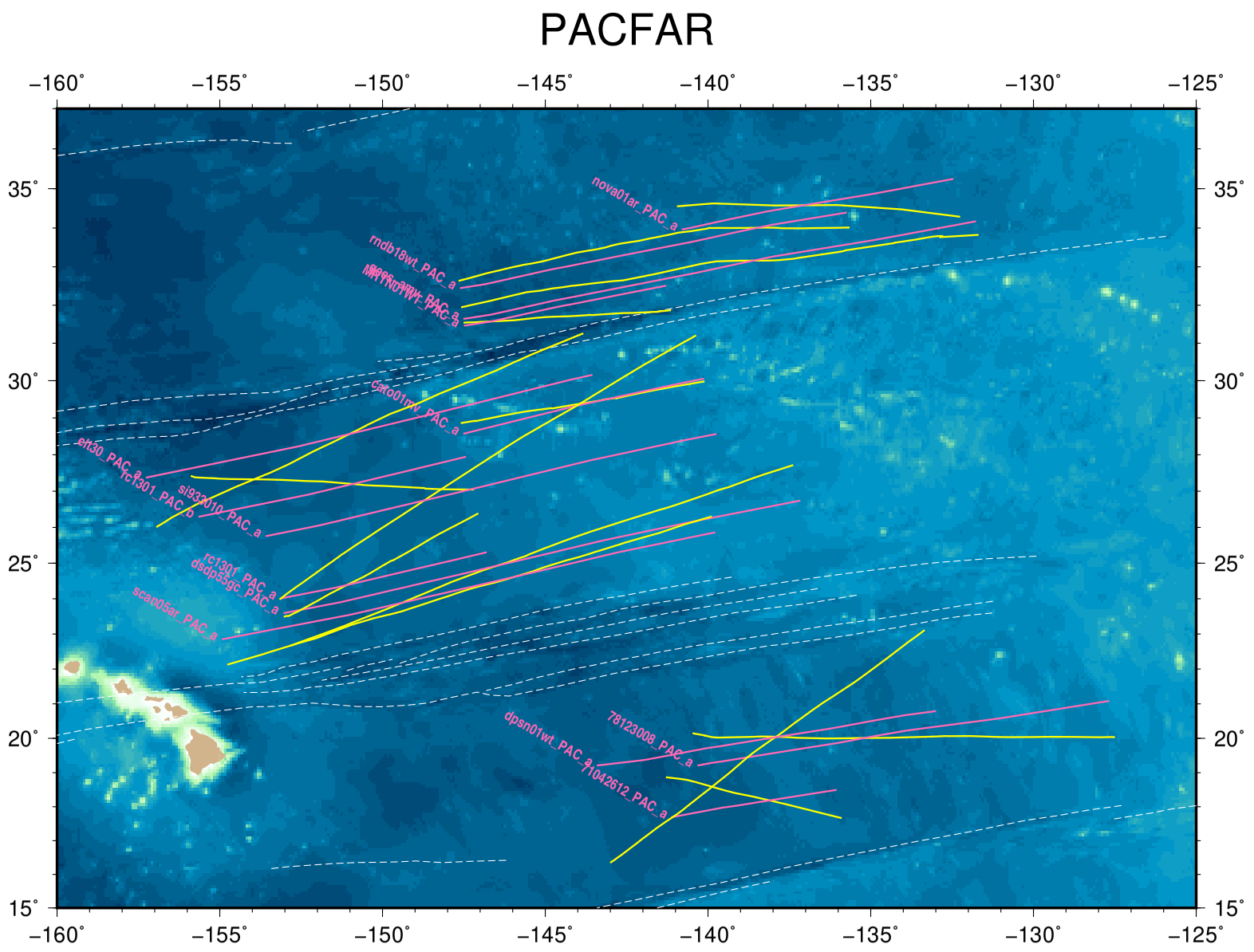

Figure S11. Original ship tracks (yellow) and tracks projected onto flow lines (magenta) in the PACFAR-PAC ridge flank region.

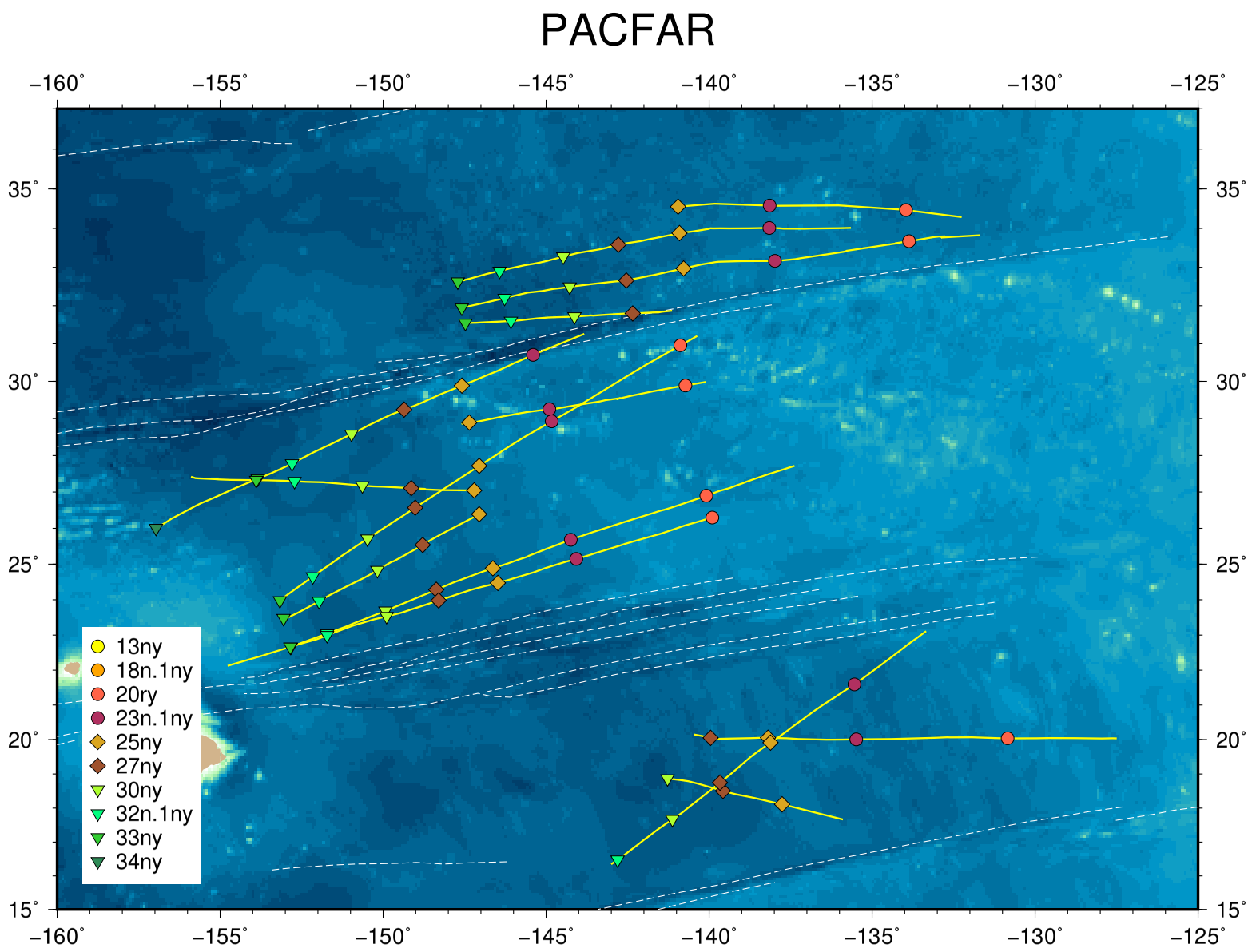

Figure S12. Location of selected magnetic block boundaries on original ship tracks in the PACFAR-PAC ridge flank region.

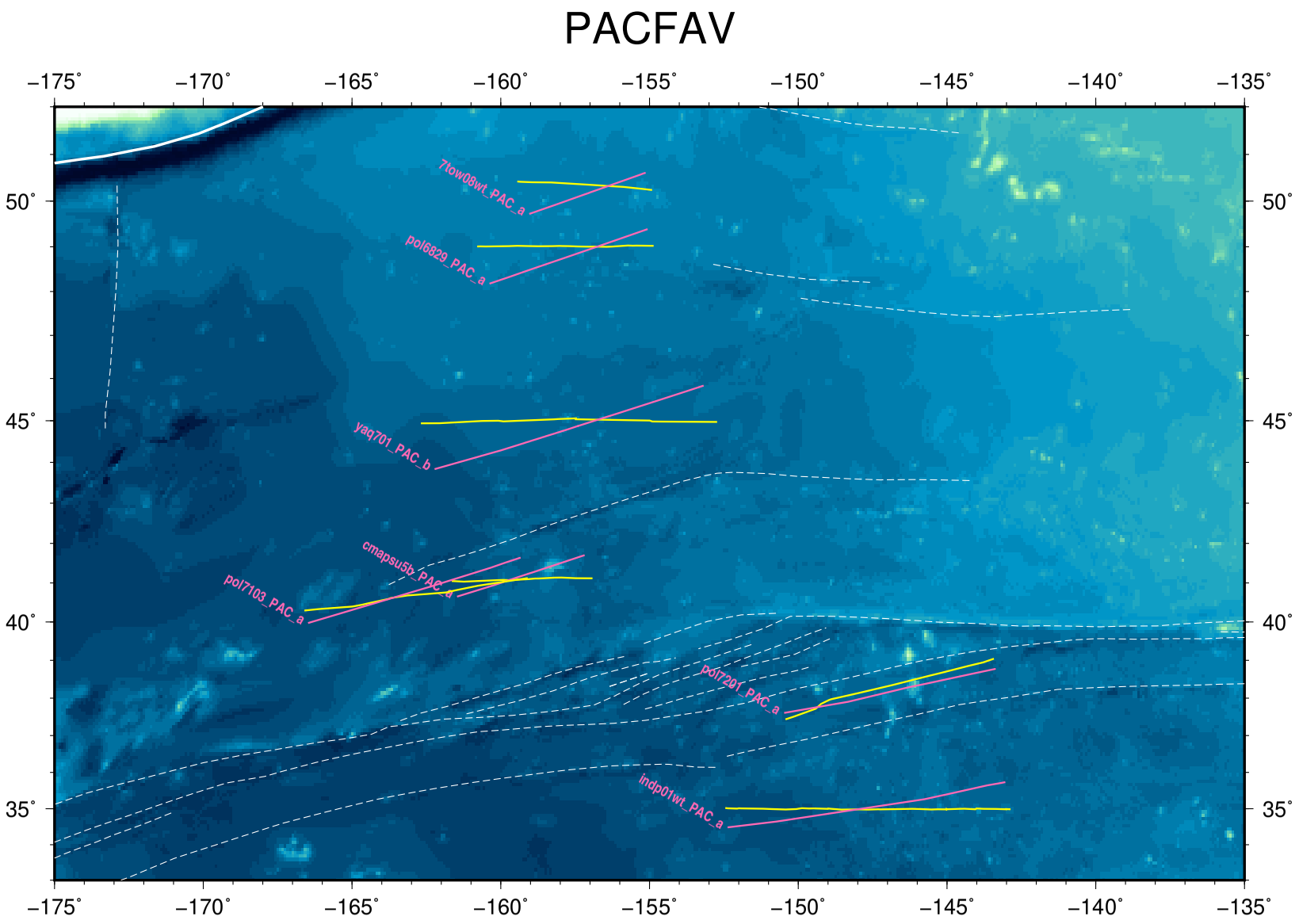

Figure S13. Original ship tracks (yellow) and tracks projected onto flow lines (magenta) in the PACFAV-PAC ridge flank region.

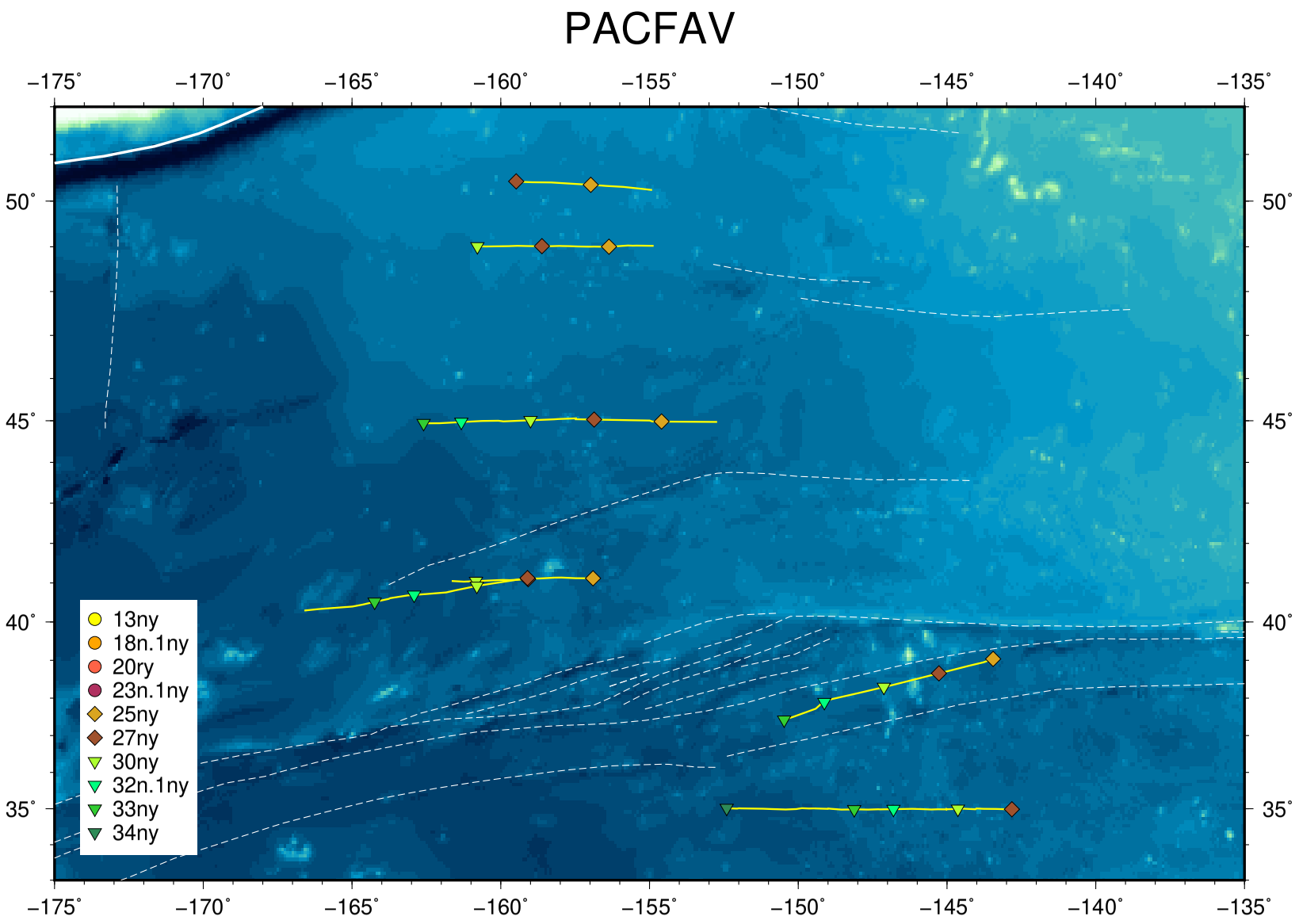

Figure S14. Location of selected magnetic block boundaries on original ship tracks in the PACFAV-PAC ridge flank region.

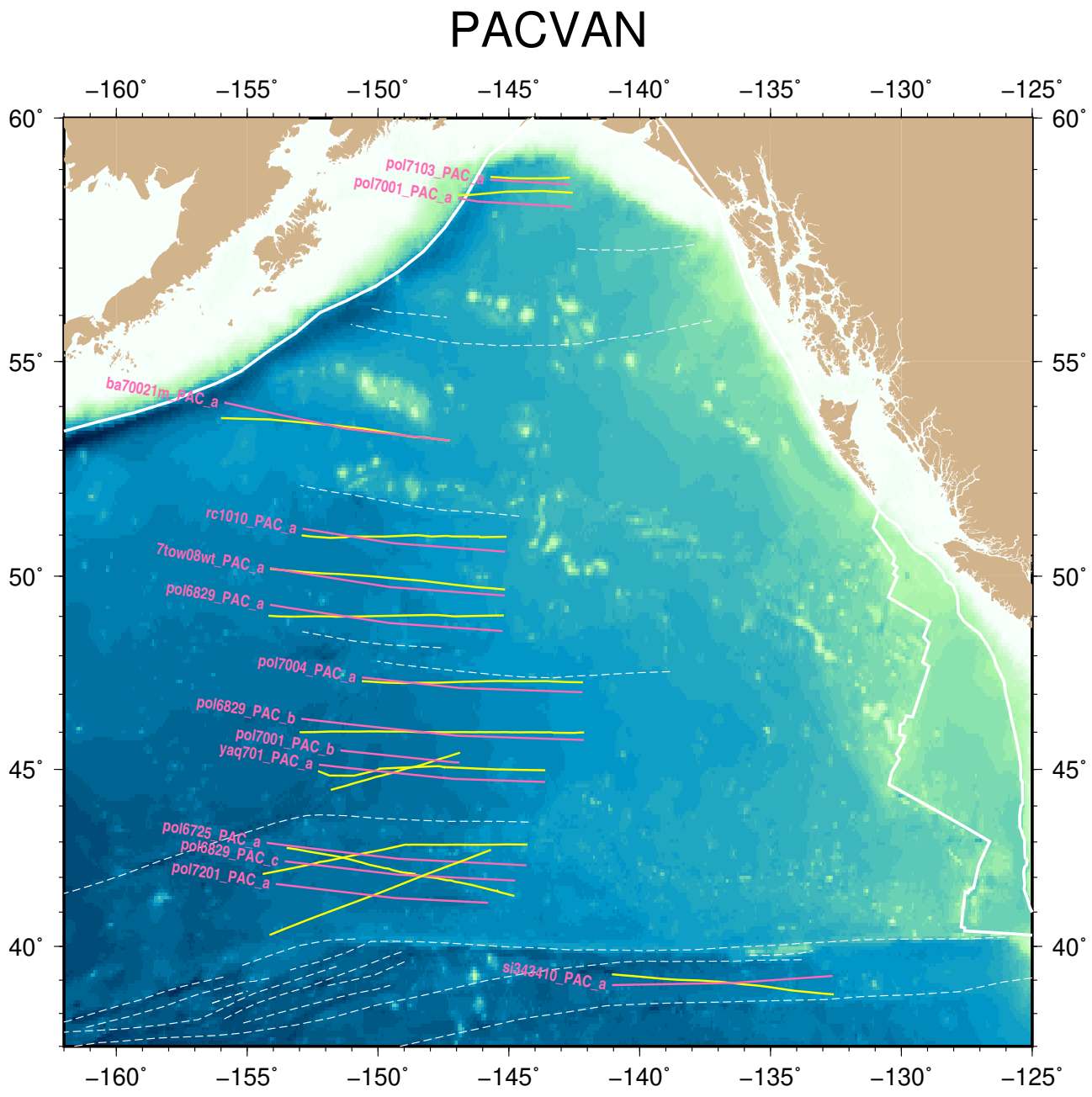

Figure S15. Original ship tracks (yellow) and tracks projected onto flow lines (magenta) in the PACVAN-PAC ridge flank region.

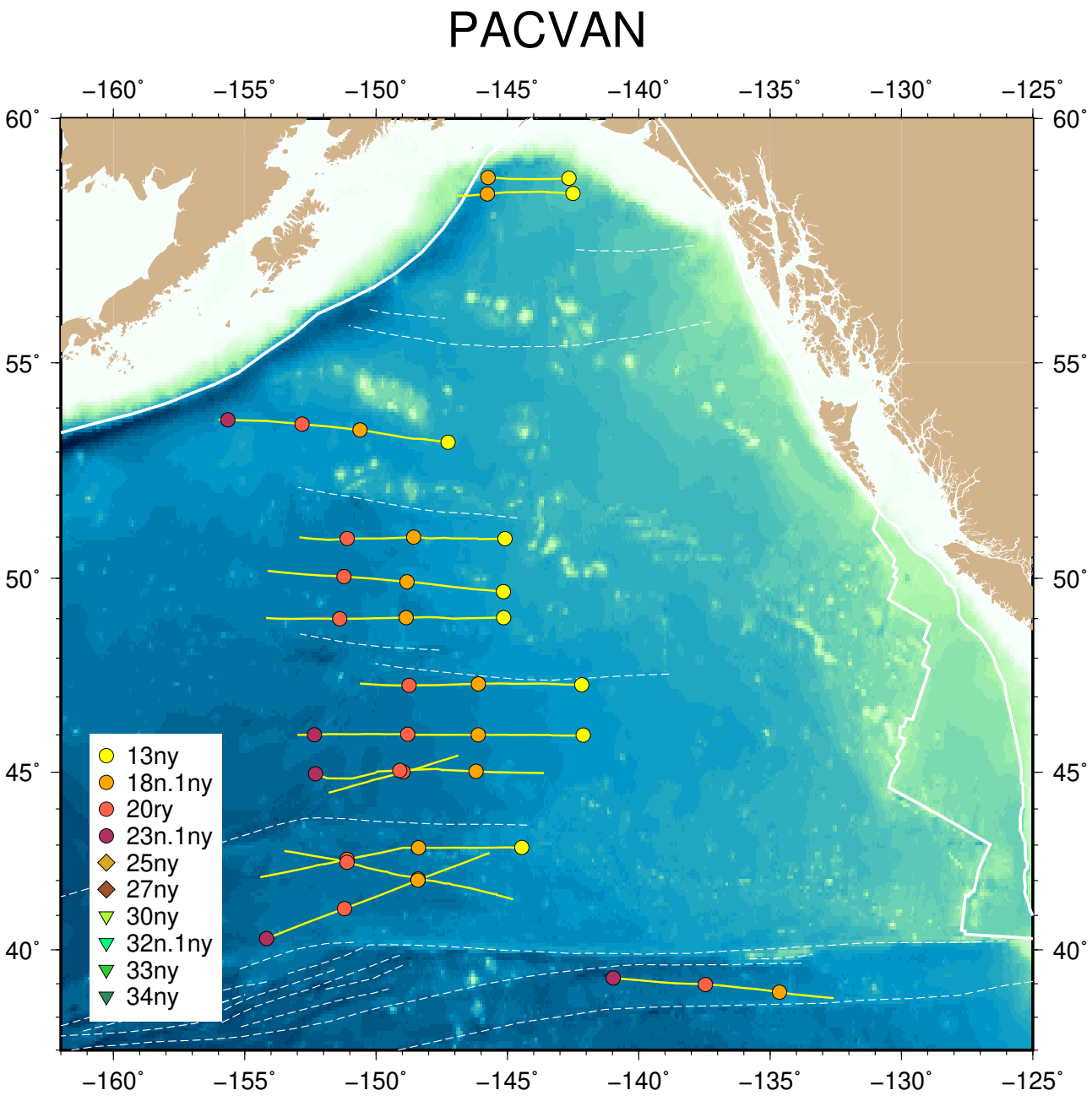

Figure S16. Location of selected magnetic block boundaries on original ship tracks in the PACVAN-PAC ridge flank region.

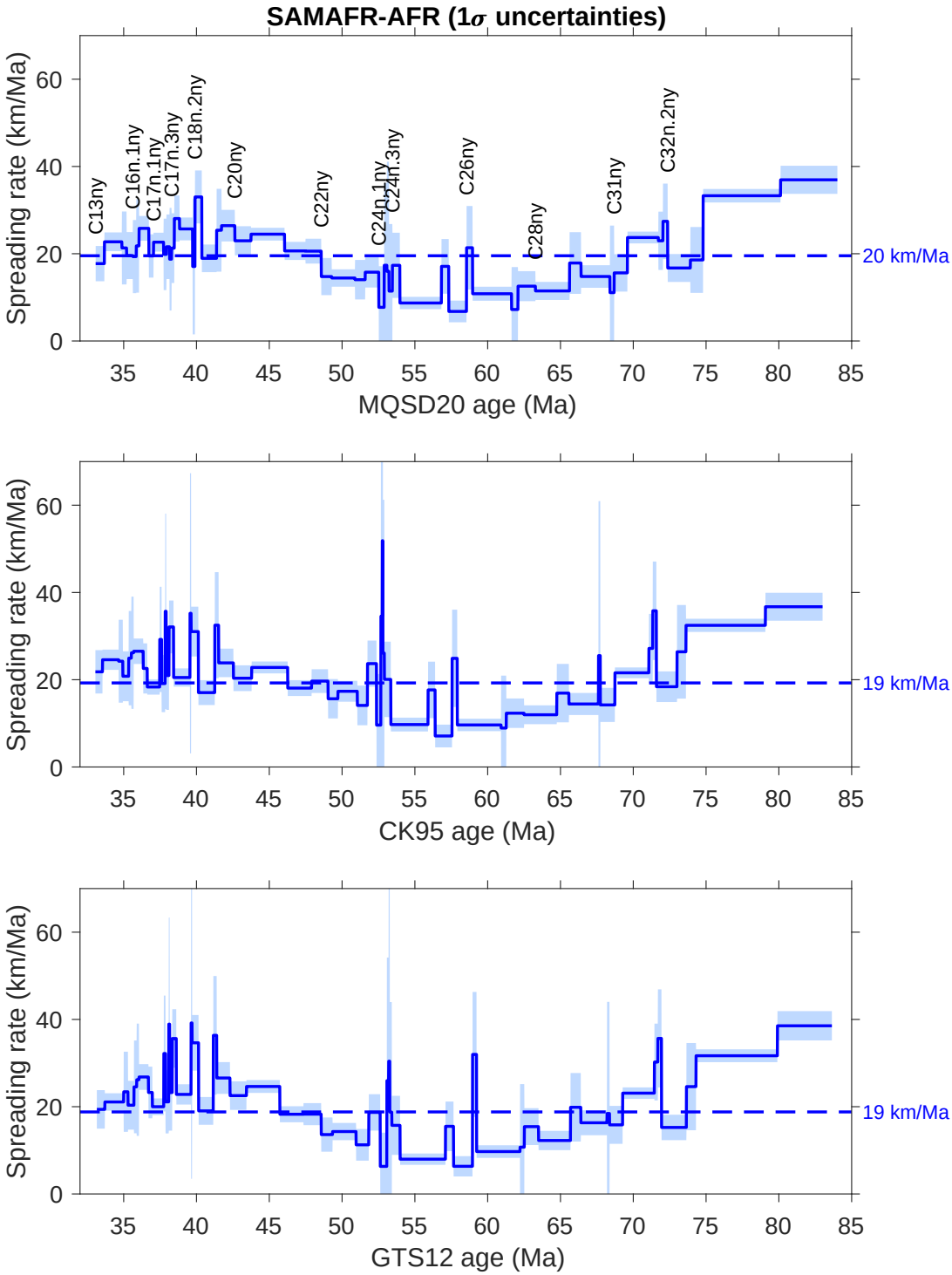

Figure S17. Half-spreading rates in the SAMAFR-AFR ridge flank region for different GPTSs: MQSD20 (this paper), CK95 (Cande & Kent 1992, 1995), and GTS12 (Ogg 2012). The shaded areas show 1σ uncertainties in spreading rate, computed from the uncertainties in BMDs as the square root of the diagonal of matrix $\mathbf{C}_1$ (Equation 7).

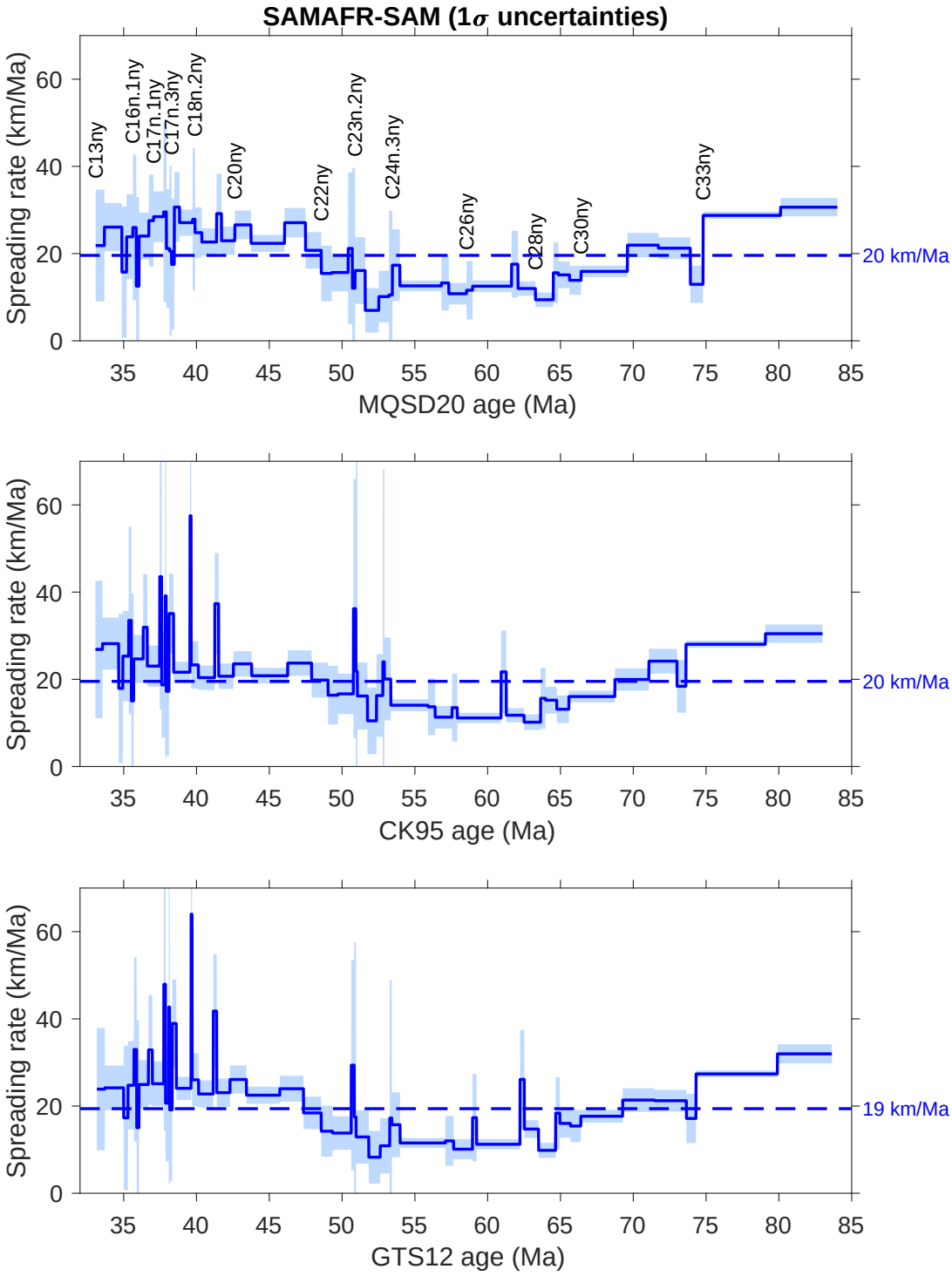

Figure S18. Half-spreading rates in the SAMAFR-SAM ridge flank region for different GPTSs: MQSD20 (this paper), CK95 (Cande & Kent 1992, 1995), and GTS12 (Ogg 2012). The shaded areas show 1σ uncertainties in spreading rate, computed from the uncertainties in BMDs as the square root of the diagonal of matrix $\mathbf{C}_1$ (Equation 7).

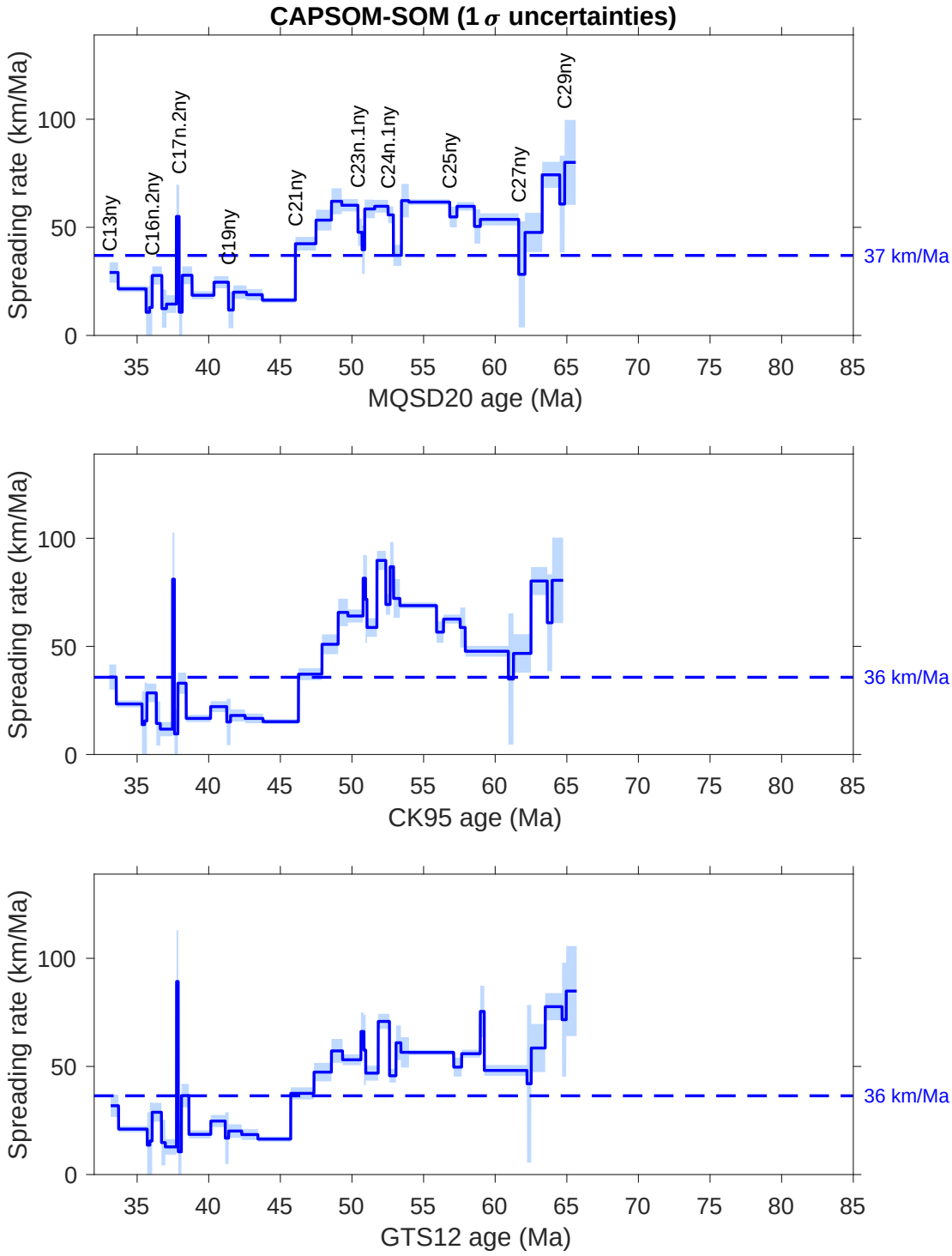

Figure S19. Half-spreading rates in the CAPSOM-SOM ridge flank region for different GPTSs: MQSD20 (this paper), CK95 (Cande & Kent 1992, 1995), and GTS12 (Ogg 2012). The shaded areas show 1σ uncertainties in spreading rate, computed from the uncertainties in BMDs as the square root of the diagonal of matrix $\mathbf{C}_1$ (Equation 7).

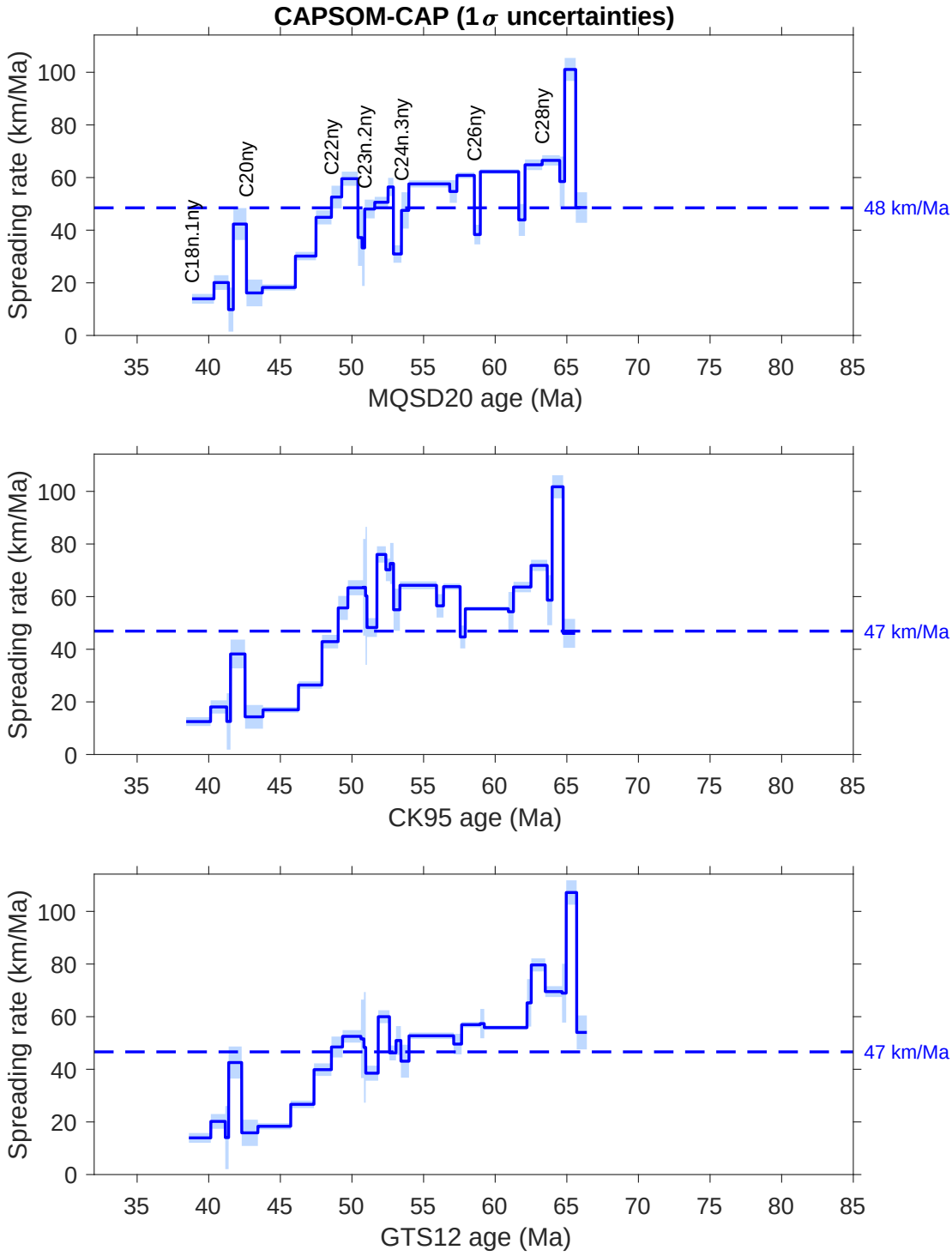

Figure S20. Half-spreading rates in the CAPSOM-CAP ridge flank region for different GPTSs: MQSD20 (this paper), CK95 (Cande & Kent 1992, 1995), and GTS12 (Ogg 2012). The shaded areas show 1σ uncertainties in spreading rate, computed from the uncertainties in BMDs as the square root of the diagonal of matrix $\mathbf{C}_1$ (Equation 7).

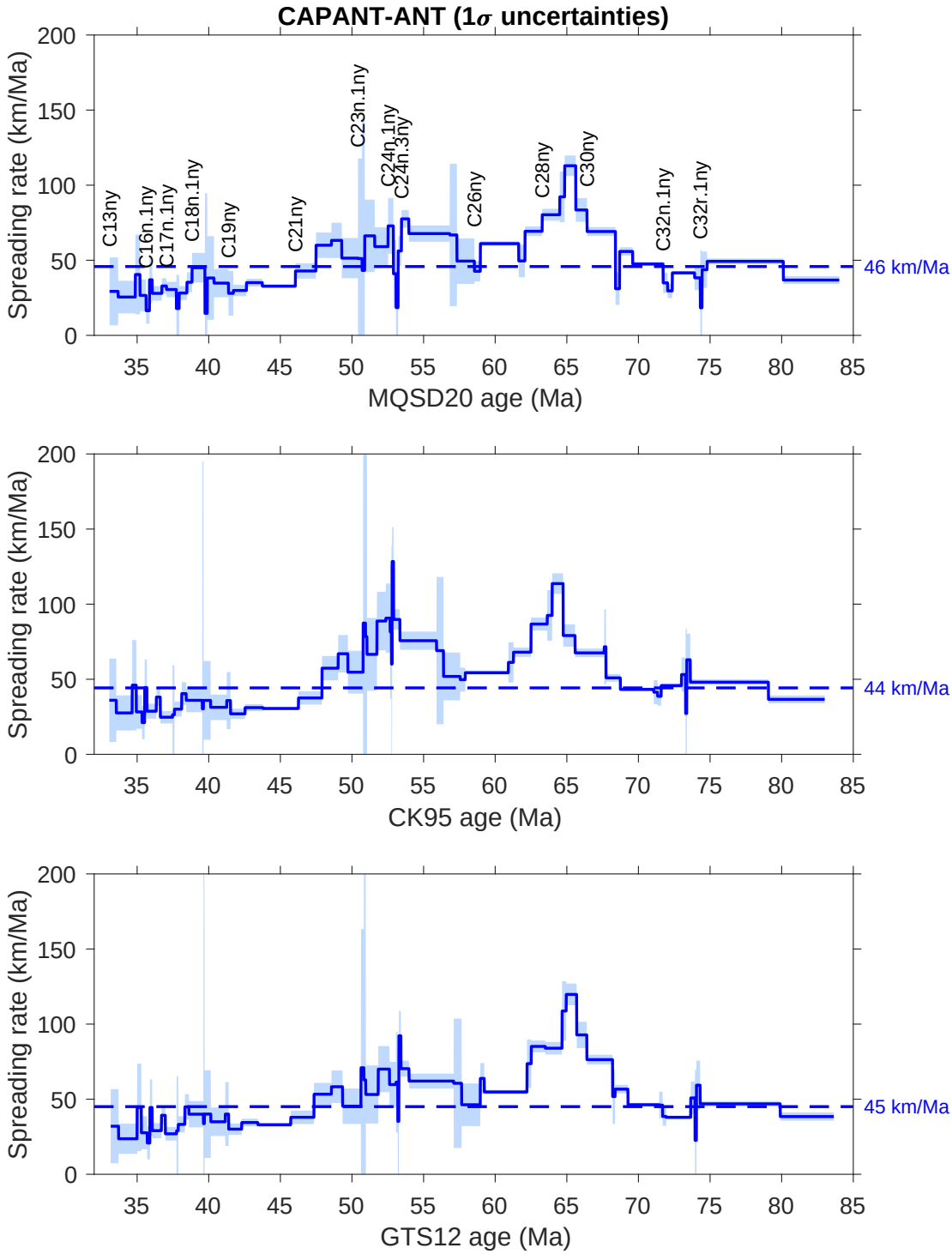

Figure S21. Half-spreading rates in the CAPANT-ANT ridge flank region for different GPTSs: MQSD20 (this paper), CK95 (Cande & Kent 1992, 1995), and GTS12 (Ogg 2012). The shaded areas show 1σ uncertainties in spreading rate, computed from the uncertainties in BMDs as the square root of the diagonal of matrix $\mathbf{C}_1$ (Equation 7).

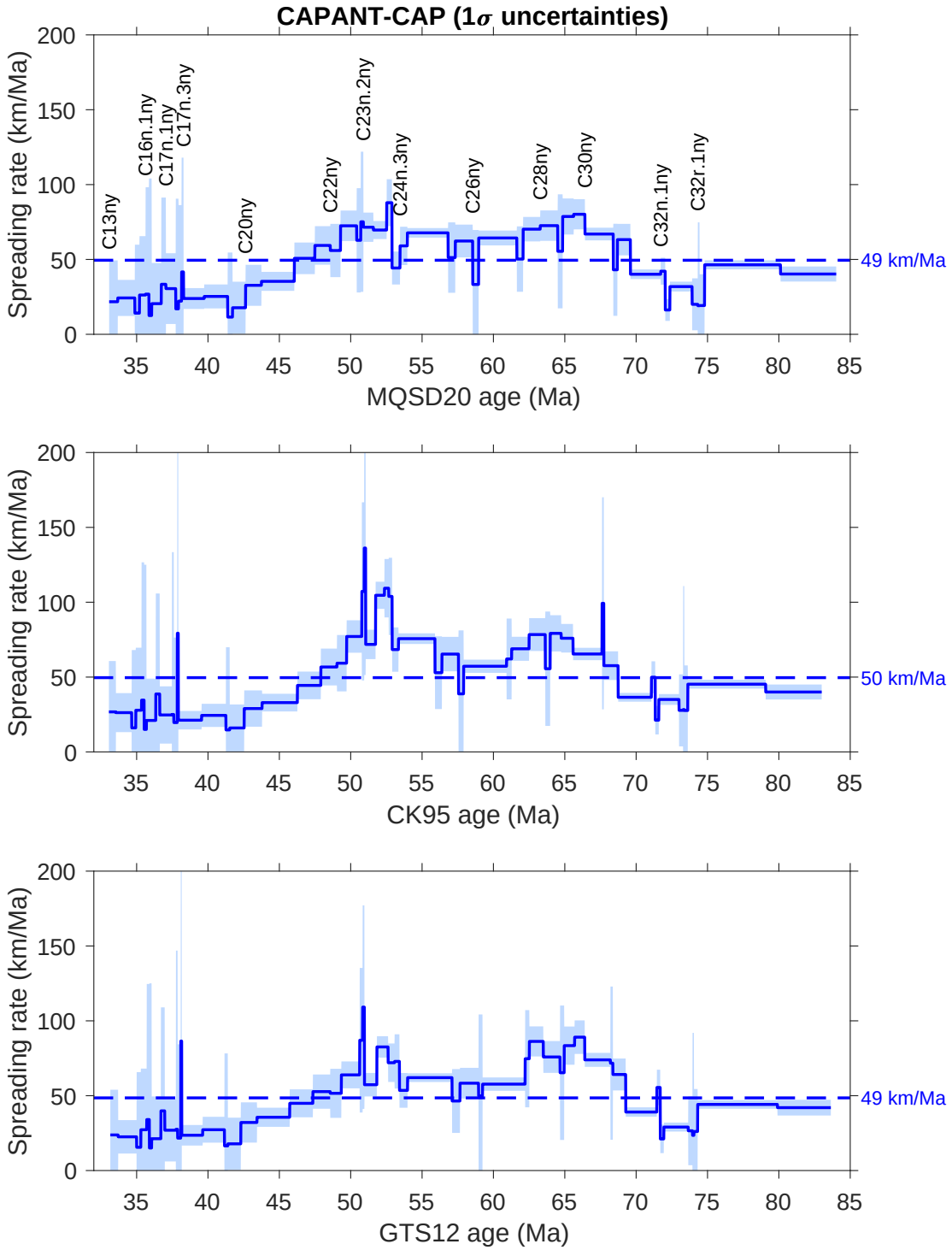

Figure S22. Half-spreading rates in the CAPANT-CAP ridge flank region for different GPTSs: MQSD20 (this paper), CK95 (Cande & Kent 1992, 1995), and GTS12 (Ogg 2012). The shaded areas show 1σ uncertainties in spreading rate, computed from the uncertainties in BMDs as the square root of the diagonal of matrix $\mathbf{C}_1$ (Equation 7).

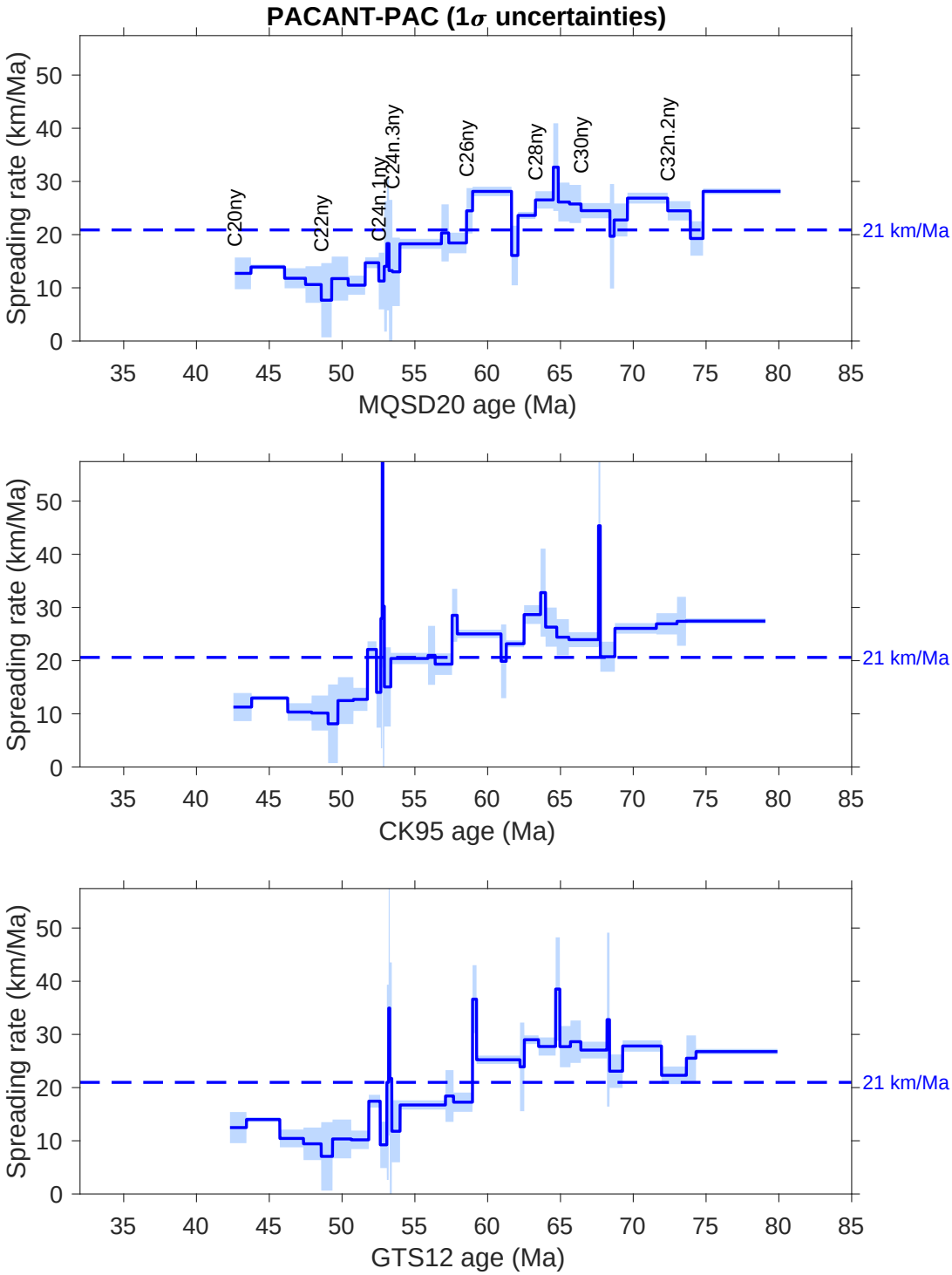

Figure S23. Half-spreading rates in the PACANT-PAC ridge flank region for different GPTSs: MQSD20 (this paper), CK95 (Cande & Kent 1992, 1995), and GTS12 (Ogg 2012). The shaded areas show 1σ uncertainties in spreading rate, computed from the uncertainties in BMDs as the square root of the diagonal of matrix $\mathbf{C}_1$ (Equation 7).

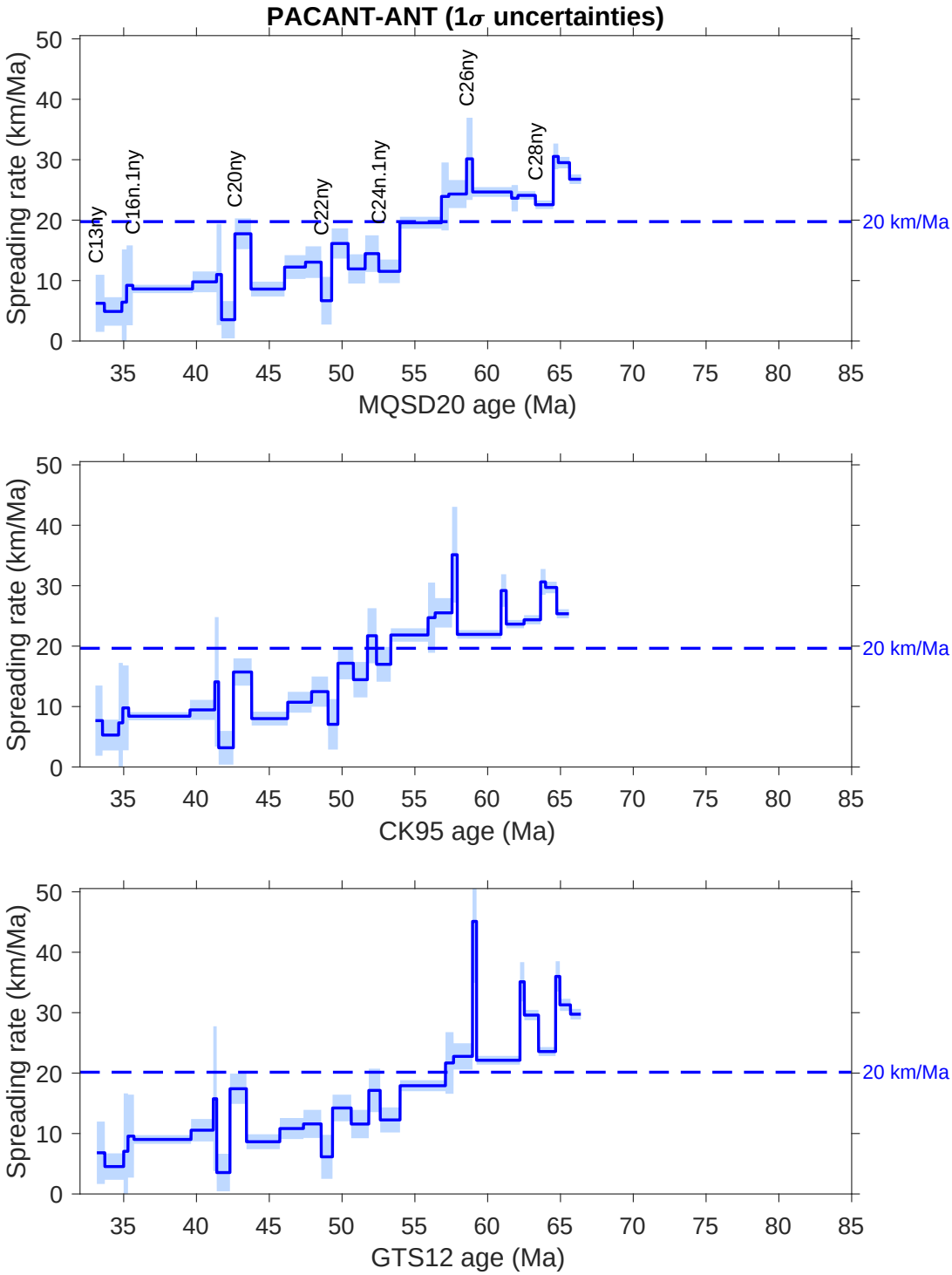

Figure S24. Half-spreading rates in the PACANT-ANT ridge flank region for different GPTSs: MQSD20 (this paper), CK95 (Cande & Kent 1992, 1995), and GTS12 (Ogg 2012). The shaded areas show 1σ uncertainties in spreading rate, computed from the uncertainties in BMDs as the square root of the diagonal of matrix $\mathbf{C}_1$ (Equation 7).

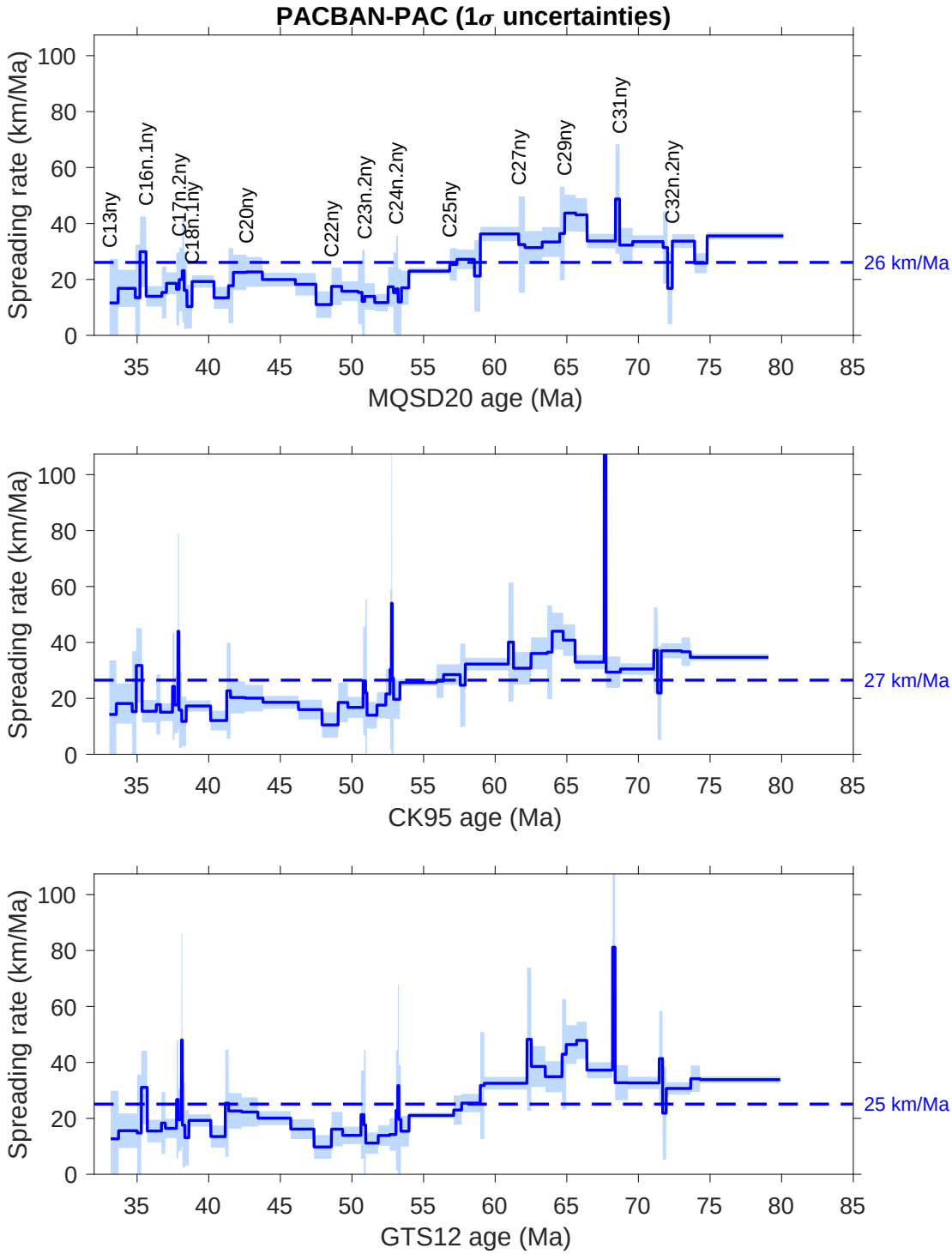

Figure S25. Half-spreading rates in the PACBAN-PAC ridge flank region for different GPTSs: MQSD20 (this paper), CK95 (Cande & Kent 1992, 1995), and GTS12 (Ogg 2012). The shaded areas show 1σ uncertainties in spreading rate, computed from the uncertainties in BMDs as the square root of the diagonal of matrix $\mathbf{C}_1$ (Equation 7).

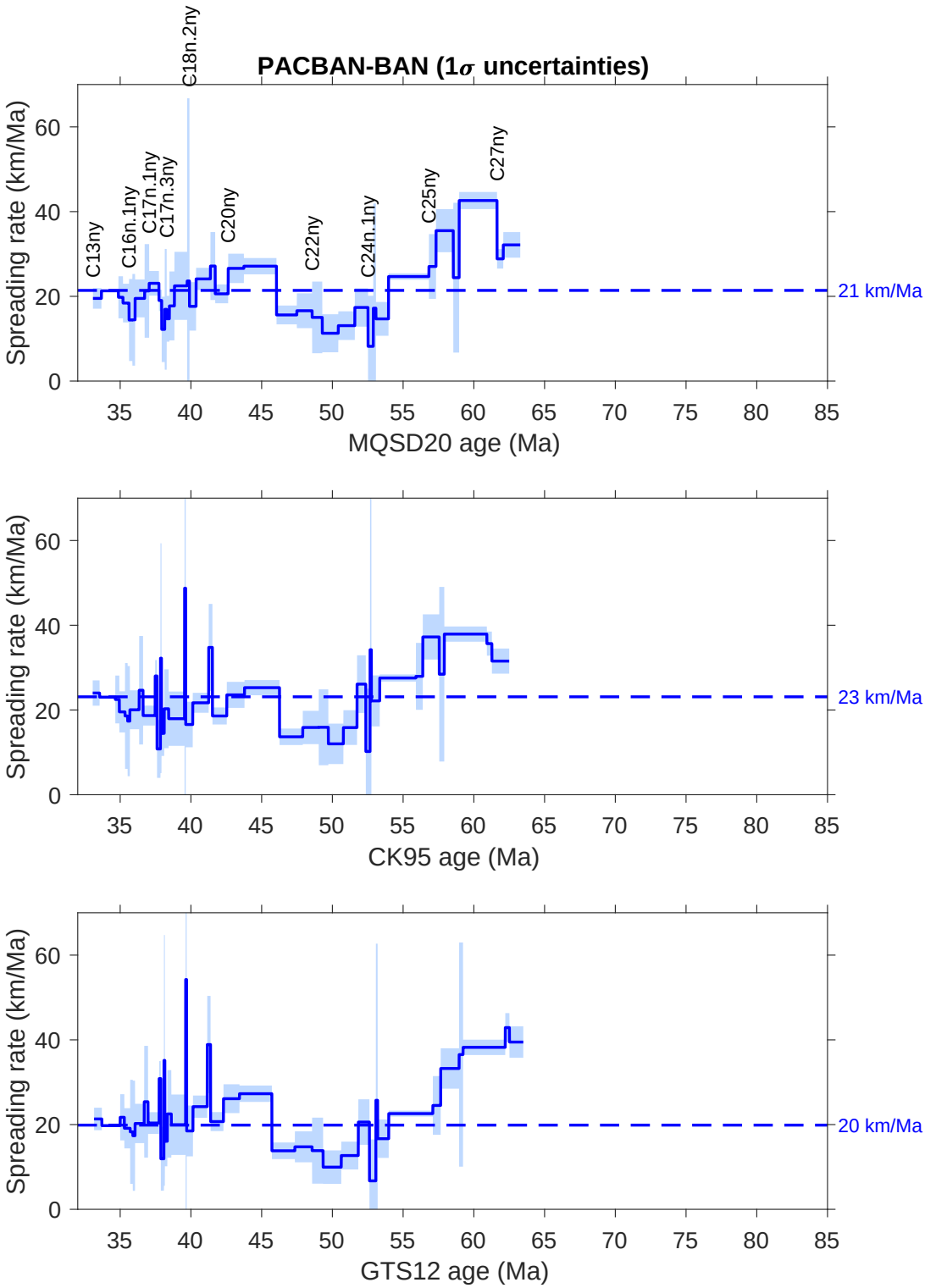

Figure S26. Half-spreading rates in the PACBAN-BAN ridge flank region for different GPTSs: MQSD20 (this paper), CK95 (Cande & Kent 1992, 1995), and GTS12 (Ogg 2012). The shaded areas show 1σ uncertainties in spreading rate, computed from the uncertainties in BMDs as the square root of the diagonal of matrix $\mathbf{C}_1$ (Equation 7).

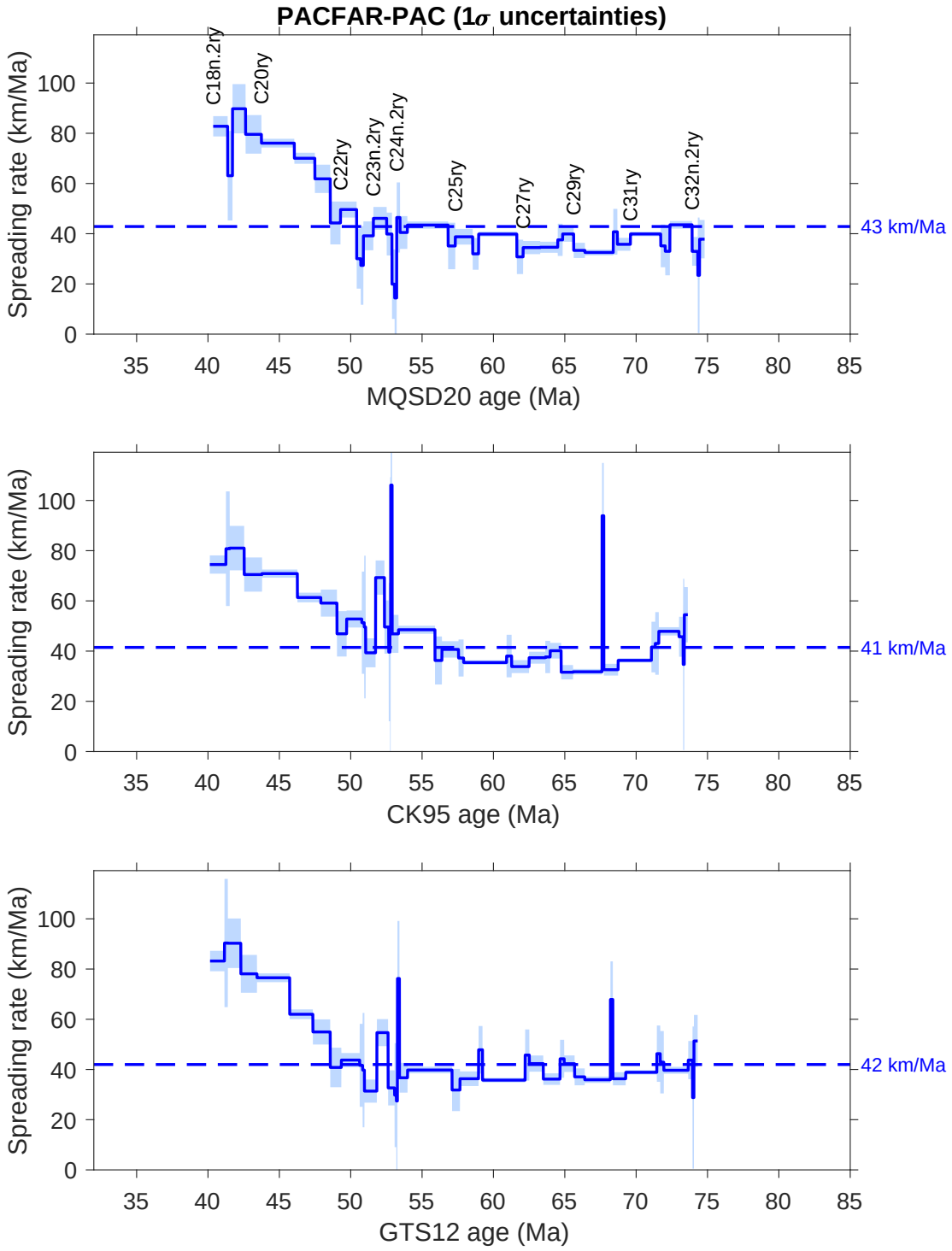

Figure S27. Half-spreading rates in the PACFAR-PAC ridge flank region for different GPTSs: MQSD20 (this paper), CK95 (Cande & Kent 1992, 1995), and GTS12 (Ogg 2012). The shaded areas show 1σ uncertainties in spreading rate, computed from the uncertainties in BMDs as the square root of the diagonal of matrix $\mathbf{C}_1$ (Equation 7).

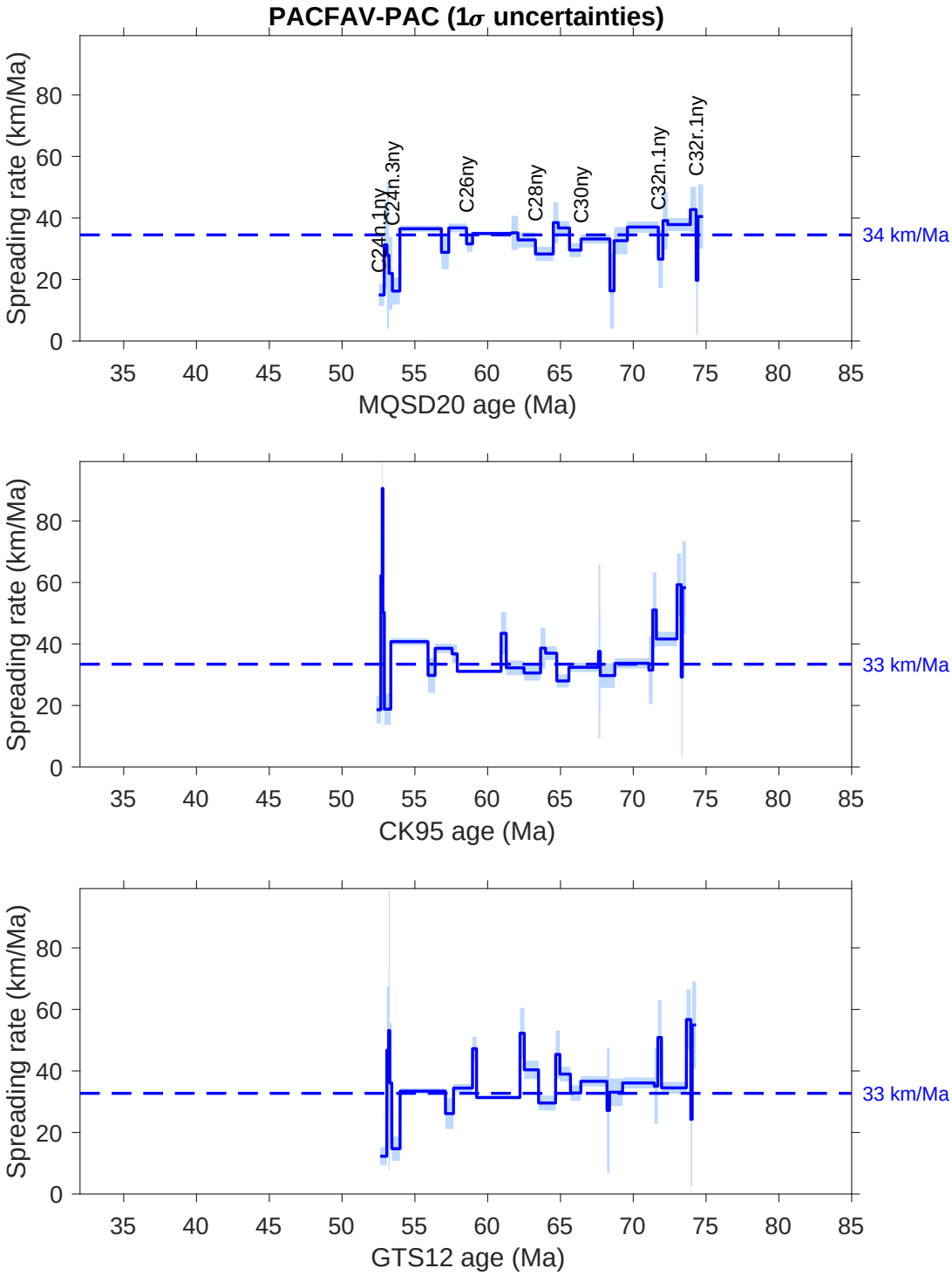

Figure S28. Half-spreading rates in the PACFAV-PAC ridge flank region for different GPTSs: MQSD20 (this paper), CK95 (Cande & Kent 1992, 1995), and GTS12 (Ogg 2012). The shaded areas show 1σ uncertainties in spreading rate, computed from the uncertainties in BMDs as the square root of the diagonal of matrix $\mathbf{C}_1$ (Equation 7).

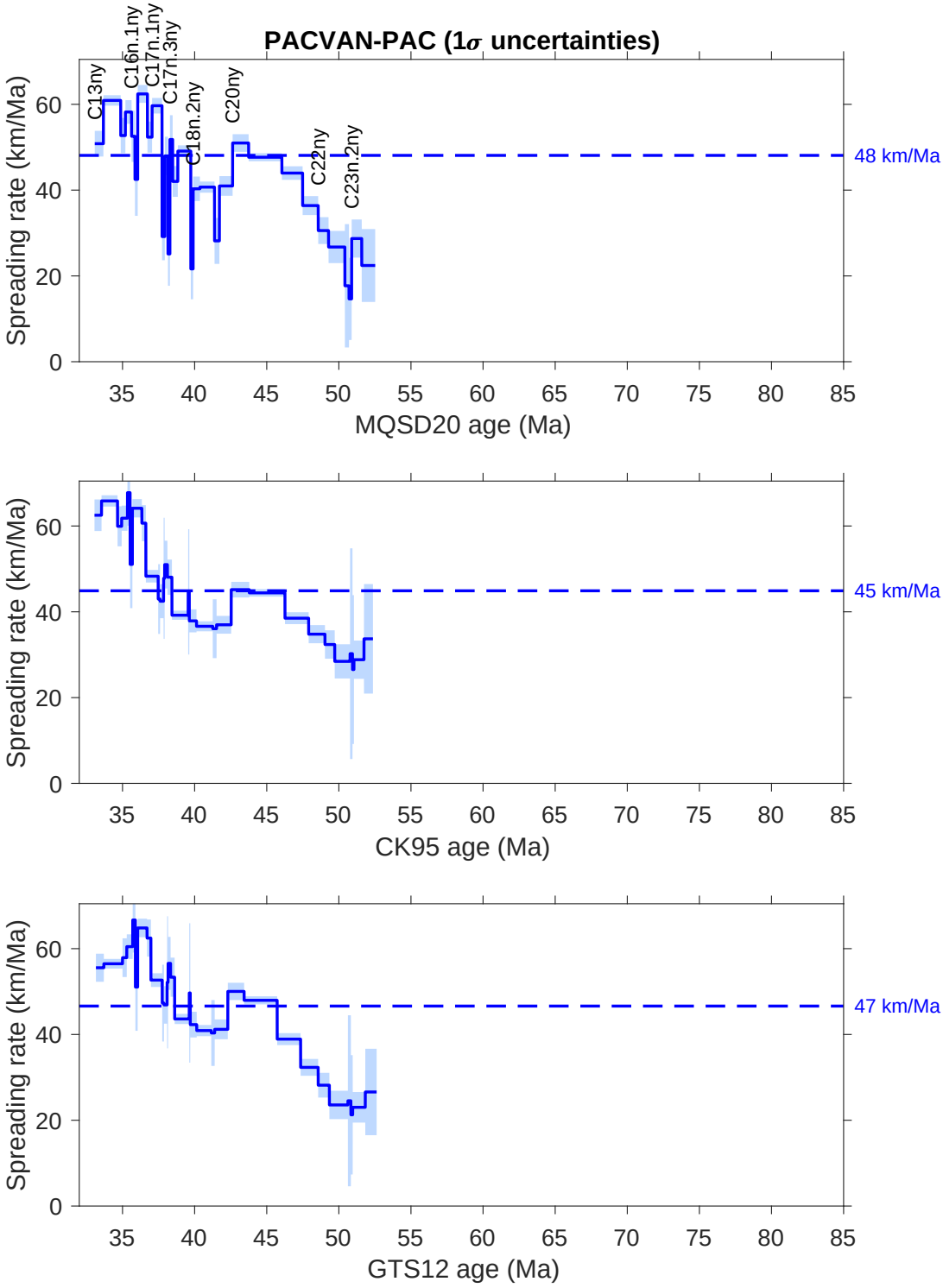

Figure S29. Half-spreading rates in the PACVAN-PAC ridge flank region for different GPTSs: MQSD20 (this paper), CK95 (Cande & Kent 1992, 1995), and GTS12 (Ogg 2012). The shaded areas show 1σ uncertainties in spreading rate, computed from the uncertainties in BMDs as the square root of the diagonal of matrix $\mathbf{C}_1$ (Equation 7).